



This is the accepted manuscript made available via CHORUS. The article has been published as:

# Driven neutron star collapse: Type I critical phenomena and the initial black hole mass distribution

Scott C. Noble and Matthew W. Choptuik

Phys. Rev. D **93**, 024015 — Published 11 January 2016

DOI: [10.1103/PhysRevD.93.024015](https://doi.org/10.1103/PhysRevD.93.024015)

# Driven neutron star collapse: Type I critical phenomena and the initial black hole mass distribution

Scott C. Noble<sup>1,\*</sup> and Matthew W. Choptuik<sup>2,†</sup>

<sup>1</sup> *Department of Physics and Engineering Physics,*

*The University of Tulsa, 800 South Tucker Drive, Tulsa, OK 74104 USA*

<sup>2</sup> *CIFAR Cosmology and Gravity Program, Department of Physics and Astronomy,  
University of British Columbia, 6224 Agricultural Road, Vancouver, Canada, V6T 1Z1*

(Dated: December 9, 2015)

We study the general relativistic collapse of neutron star (NS) models in spherical symmetry. Our initially stable models are driven to collapse by the addition of one of two things: an initially ingoing velocity profile, or a shell of minimally coupled, massless scalar field that falls onto the star. Tolman-Oppenheimer-Volkoff (TOV) solutions with an initially isentropic, gamma-law equation of state serve as our NS models. The initial values of the velocity profile’s amplitude and the star’s central density span a parameter space which we have surveyed extensively and which we find provides a rich picture of the possible end states of NS collapse. This parameter space survey elucidates the boundary between Type I and Type II critical behavior in perfect fluids which coincides, on the subcritical side, with the boundary between dispersed and bound end states. For our particular model, initial velocity amplitudes greater than  $0.3c$  are needed to probe the regime where arbitrarily small black holes can form. In addition, we investigate Type I behavior in our system by varying the initial amplitude of the initially imploding scalar field. In this case we find that the Type I critical solutions resemble TOV solutions on the 1-mode unstable branch of equilibrium solutions, and that the critical solutions’ frequencies agree well with the fundamental mode frequencies of the unstable equilibria. Additionally, the critical solution’s scaling exponent is shown to be well approximated by a linear function of the initial star’s central density.

PACS numbers: 04.25.Dm, 04.40.Dg, 97.60.Jd, 97.60.Lf

## I. INTRODUCTION

The dynamics of compact gravitating objects out of equilibrium has always been a topic of much interest in astrophysics. Physical systems that fall under this subject include supernovae, “failed” supernovae such as hypernovae or collapsars, gamma-ray burst (GRB) progenitors, coalescing binary neutron star (NS) systems, accreting compact stars, and NSs that undergo sudden phase transitions, to name only a few. In the case of a core collapse supernova, a NS may form and undergo additional evolution. For instance, the outwardly-moving shock wave of matter from the supernova may stall and collapse onto the nascent neutron core [1]. In contrast, if the NS is in a binary system with a less compact companion star, accretion from the companion may push the NS over its Chandrasekhar limit. In either of these cases, the resultant non-equilibrium system will most likely undergo a hydrodynamic implosion that will often result in black hole formation.

Here we wish to present work that sets such excited NSs in the context of critical phenomena in general relativity. Specifically, we wish to investigate 1) the criteria required to initiate black hole formation, the boundary

between black hole forming scenarios and those that do not form black holes, and 2) the dynamical behavior of the systems in general. This work is one of only several to date that ties critical phenomena to astrophysical scenarios [2–6, 63, 64, 67–69].

We are certainly not the first to study numerical evolutions of NS models far from equilibrium. For example, Shapiro and Teukolsky [7] asked whether a stable NS with a mass below the Chandrasekhar mass could be driven to collapse by compression. With a mixed Euler-Lagrangian code, they began to answer the question by studying stable stars whose density profiles had been “inflated” in a self-similar manner such that the stars became larger and more massive. Due to insufficient central pressure, such configurations were no longer equilibrium solutions and inevitably collapsed. By increasing the degree to which the equilibrium stars were inflated, they were able to supply more kinetic energy to the system. They found that black holes formed only for stars with masses greater than the maximum equilibrium mass. In addition, Shapiro and Teukolsky studied accretion induced collapse, where it was again found that collapse to a black hole occurred only when the total mass of the system—in this case the mass of the star *and* the mass of the accreting matter—was above the maximum stable mass. Both examples seemed to suggest that even driven stars needed to have masses above the maximum stable mass in order to produce black holes. Moreover, they only witnessed three types of outcomes: 1) homologous bounce, wherein the entire star underwent a bounce after imploding to maxi-

---

\*Electronic address: [scott-noble@utulsa.edu](mailto:scott-noble@utulsa.edu); URL: <http://personal.utulsa.edu/~scn759/>

†Electronic address: [choptuik@physics.ubc.ca](mailto:choptuik@physics.ubc.ca); URL: <http://laplace.physics.ubc.ca/People/matt/>

imum compression; 2) non-homologous bounce where less than 50% of the matter followed a bounce sequence; and 3) direct collapse to a black hole. Also, Baumgarte et al. [8] using a Lagrangian code based on the formulation of Hernandez and Misner [9] qualitatively confirmed these results.

In order to investigate the question posed by Shapiro and Teukolsky further, Gourgoulhon [10, 11] used pseudo-spectral methods and realistic, tabulated equations of state to characterize the various ways in which a NS may collapse when given an *ad hoc*, polynomial velocity profile. Such velocity profiles mimic those seen in core collapse simulations as described in [12, 13]. Given a sufficiently large amplitude of the profile, Gourgoulhon was able to form black holes from stable stars with masses well below the maximum. He was also able to observe bounces off the inner core, but was unable to continue the evolution significantly past the formation of the shock since spectral techniques typically behave poorly for discontinuous solutions.

To further explore this problem and resolve the shocks more accurately, Novak [6] used a Eulerian code with High-Resolution Shock-Capturing (HRSC) methods. In addition, he surveyed the parameter space in the black hole-forming regime in much greater detail than previous studies, illuminating a new scenario in which a black hole may form on the same dynamical time-scale as the bounce. Depending on the amplitude of the velocity perturbation, such cases can lead to black holes that have smaller masses than their progenitor stars. This dependence suggested that masses of black holes generated by NS collapse might not be constrained by the masses of their parents and, consequently, could—in principle—allow the black hole mass,  $M_{\text{BH}}$ , to take on a continuum of values. In addition, in accordance with the study described in [10], Novak found that the initial star did not have to be more massive than the maximum mass in order to evolve to a black hole. In fact, he found that for two equations of state—the typical polytropic equation of state (EOS) and a realistic EOS described in [14]—arbitrarily small black holes could be made by tuning the initial amplitude of the velocity profile about the value at which black holes are first seen. Hence, Novak’s work suggests that black holes born from NSs are able to have masses in the range  $0 < M_{\text{BH}} \leq M_*$ , where  $M_*$  is the mass of the progenitor star. This suggests that critical phenomena may play a role in the black hole mass function of driven NSs.

Critical phenomena in general relativity involves the study of the solutions—called *critical* solutions—that lie at the boundary between black hole-forming and black hole-lacking spacetimes (for reviews please see [15–17]). General relativistic critical phenomena began with a detailed numerical investigation of the dynamics of a minimally coupled, massless scalar field in spherical symmetry [18]. This first study identified three fundamental features of the critical behavior: 1) universality and 2) scale invariance of a critical solution that arises at thresh-

old, with 3) power-law scaling behavior in the vicinity of threshold. All three of these have now been seen in a multitude of collapse models with a wide variety of matter sources, including perfect fluids [19, 20, 22], an SU(2) Yang-Mills model [23, 24], and collisionless matter [25, 26] to cite just a few. It was eventually found that there are two related yet distinct types of critical phenomena, dubbed Type I and Type II, due to similarities between the critical phenomena observed in gravitational collapse, and those familiar from statistical mechanics.

Type II behavior entails critical solutions that are either continuously self-similar (CSS) or discretely self-similar (DSS). Supercritical solutions—those that form black holes—give rise to black holes with masses,  $M_{\text{BH}}(p)$ , that scale as a power-law,

$$M_{\text{BH}}(p) \propto |p - p^*|^\gamma, \quad (1)$$

implying that arbitrarily small black holes can be formed. Here,  $p$  parameterizes a 1-parameter family of initial data with which one can tune toward the critical solution, located at  $p = p^*$ , and  $\gamma$  is the scaling exponent of the critical behavior. Since  $M_{\text{BH}}(p)$  is, loosely speaking, continuous across  $p = p^*$ , this type of critical behavior was named “Type II” since it parallels Type II (continuous) phase transitions in statistical mechanics.

As in the statistical mechanical case, there is a Type I behavior, where the black hole mass “turns on” at a finite value. Type I critical solutions are quite different from their Type II counterparts, tending to be metastable star-like solutions that are either static or periodic. The critical solutions can therefore be described by a continuous or discrete symmetry in time, analogous to the Type II CSS and DSS solutions. Unlike the Type II case, however, the black hole masses of supercritical solutions do not follow a power-law scaling. Instead, the span of time,  $\Delta T_0(p)$ —as measured by an observer at the origin—that a given solution is close to the critical solution scales with the solution’s deviation in parameter space from criticality

$$\Delta T_0(p) \propto -\sigma \ln |p - p^*|, \quad (2)$$

where  $\sigma$  is the scaling exponent of Type I behavior.

We note that many of the features of critical gravitational collapse can be understood in a manner that also has a clear parallel in statistical mechanical critical phenomena. In particular, the critical solutions that have been identified to date, although unstable, tend to be minimally so in the sense that they have only a single unstable mode in perturbation theory [20, 21]. The Lyapunov exponent associated with this mode can then be directly related to the lifetime-scaling exponent,  $\sigma$ , for Type I solutions, and to the mass-scaling exponent,  $\gamma$ , for Type II solutions.

In collapse models that involve matter characterized by one or more intrinsic length scales, the possibility of both types of critical behavior arises. Indeed, the boundary separating the two types has been studied extensively

in the SU(2) Einstein-Yang-Mills model [23, 24] as well as the Einstein-Klein-Gordon system [27]. In the latter case it was found that when the length scale  $\lambda$ —which characterized the “spatial extent” of a 2-parameter family of initial data—was small compared to the scale set by the massive scalar field, Type II behavior was observed. The transition from Type II to Type I behavior was calculated for different families and was found to occur when  $\lambda m \approx 1$ , where  $m$  is the (particle) mass of the scalar field.

Two studies particularly close in spirit to our current work are due to Hawley and Choptuik [28] and Lai and Choptuik [31]. Instead of perturbing TOV solutions [39–41], these authors perturbed stable, spherically symmetric, boson stars. Boson stars are self-gravitating configurations of a complex scalar field with some prescribed self-interaction (possibly just a mass term), whose only time-dependence is a phase that varies linearly with time (see [29] and [30] for reviews). For a given self-interaction, one can generically construct one-parameter families of boson stars, where the family parameter can conveniently be taken to be the central modulus,  $\phi(0)$ , of the complex field, and which plays the role of the central rest-mass density in TOV solutions. As with their hydrostatic counterparts (discussed in more detail in Sec. II C), when the total mass,  $M_*(\phi(0))$ , of the configurations is plotted as a function of  $\phi(0)$ , one typically finds a maximum mass for some  $\phi(0) = \phi_{\max}(0)$  which signals a change in dynamical stability: stars with  $\phi(0) < \phi_{\max}(0)$  are stable, while those with  $\phi(0) > \phi_{\max}(0)$  are unstable. Additionally, for any family of boson stars, there is generally a branch of unstable stars—with  $\phi(0)$  ranging from  $\phi_{\max}$  to the next value where the mass function is a local minimum—that have precisely one unstable mode in perturbation theory. These stars are thus candidates to be Type I critical solutions in a collapse scenario.

Hawley and Choptuik perturbed a boson star by collapsing a spherical pulse of massless scalar field onto it from a distance sufficient to ensure that the two matter distributions were initially non-overlapping. As such a pulse collapses through the origin, the energy distributions associated with the two matter fields interact solely through the gravitational field. For sufficiently large amplitudes of the scalar field, the resulting increase in curvature within the star is enough to significantly compress it, ultimately resulting in either black hole formation or a star that executes a sequence of oscillations, often of large amplitude. By tuning the initial amplitude of the scalar field, Type I critical solutions were found and, per the above observation, were identified as (perturbed) one-mode unstable boson star configurations. It was verified that the lifetimes of near-critical evolutions scaled according to (2), and that in each case the scaling exponent,  $\sigma$ , was consistent with the inverse of the real part of the Lyapunov exponent,  $\omega_{Ly}$ , of the critical solution. Furthermore, values of  $\omega_{Ly}$  were independently calculated for several cases by applying linear perturbation theory to the static boson star backgrounds, and were shown to be in good agreement with those measured from the fully

dynamical calculations. Finally, since boson stars model many of the characteristics of TOV solutions, it was conjectured that the observed critical behavior would carry over to the fluid case.

We note that in the results reported in [28] the end state of marginally subcritical collapse was *not* identified as a periodic spacetime (i.e. a perturbed boson star); rather, it was assumed that the stars would disperse to spatial infinity in such cases. Upon evolving subcritical configurations for longer physical times, Lai and Choptuik [31]—in work performed simultaneously to that of [51]—found that the end states were, in fact, gravitationally bound and oscillatory. These results were subsequently verified by Hawley [32]. Interestingly, in both studies it was found that during the non-trivial gravitational interaction of the massless scalar field and the boson star there was a transfer of mass-energy from the massless scalar field to the complex scalar field, resulting in an increase of the gravitating mass of the boson star.

Returning now to the fluid case, Siebel et al. [37] sought to measure the maximum NS mass allowed by the presence of a perturbing pulse of minimally-coupled, massless scalar field. A general relativistic hydrodynamic code using a characteristic formulation was used to investigate the spherically symmetric system. However, instead of varying the massless scalar field they studied five distinct star solutions having a range of central densities that straddled the threshold of black hole formation. They found that the perturbation either led to a black hole or to oscillations of the star about its initial configuration. Further, in order to test their new 3-dimensional general relativistic fluid code, Font et al. [38] dynamically calculated the fundamental and harmonic mode frequencies of spherical TOV solutions. They observed the transition of a TOV solution on the *unstable* branch to the stable branch by evolving an unstable solution that was perturbed at the truncation error level. The unstable star overshoot and then oscillated about the stable solution, contradicting a common assumption in the field that stars from the unstable branch always formed black holes. Evolving from initial conditions consisting of an unstable TOV star has continued to be used for code-testing purposes [70]. In [67] Liebling et al. performed a similar study with weakly magnetized unstable TOV solutions in 3-d, but employed explicit and tunable perturbations to the pressure and density. They, too, found evidence for Type I behavior, though were unable to tune sufficiently close to the threshold to demonstrate the expected scaling behavior. All the different kinds of perturbations they employed drove the system to the same, seemingly *universal* solution. Proximity to the critical threshold was improved in [68], wherein they perturbed axisymmetric unstable TOV stars by truncation error and a small ingoing velocity distribution, while tuning with the central density of the star.

Apart from the work presented here (and here [51]), the most exhaustive explorations of Type I behavior involving NSs are that of Jin and Suen [63], Wan et al. [64–

66], and Kellerman, Radice, and Rezzolla [69]. The results presented in these papers indicated that the head-on axisymmetric collision of two NSs can be tuned with a variety of initial data parameters to a critical threshold that bifurcates end states involving either a single black hole or a single more massive oscillating NS. Universality of the critical behavior was supported by tuning separately the initial magnitude of the stellar velocities, central densities and adiabatic index of their polytropic EOS. Threshold solutions were found to high precision for all three of the tuning variables. All threshold solutions were found to be perturbed TOV solutions on the unstable branch, no matter the tuning parameter. Since changes in the adiabatic index may mimic the effects of cooling and accretion, an interesting conjecture was made that critical behavior might be realizable without the need for fine tuning [63]. Further, frequencies at which the near-threshold solution oscillated were measured and found to differ—by one to two orders of magnitude—from the frequencies of the  $l = 0, 1$  perturbation modes about the *initial stable* TOV solution [64]. The seeming discrepancy in frequencies was eventually explained by [69] when they demonstrated that the near-threshold solutions were perturbed TOV solutions on the unstable branch, and that the oscillations occurred at the fundamental mode of the unstable TOV solution—not the original stable TOV solution. This realization in the literature paralleled conclusions made years before in the boson star context [31], and in the TOV context [51].

In this work, we investigate both types of critical behavior using a perfect fluid model, although we focus for the most part on the Type I case. For the first time with TOV solutions, we demonstrate that the scaling exponent,  $\sigma$ , is consistent with the inverse of the real part of the Lyapunov exponent,  $\omega_{Ly}$ , of the critical solution. This provides further evidence to support the notion that the Type I critical solutions are perturbed TOV solutions on the unstable branch. The initial conditions which we adjust entail a stable TOV star with the stiffest causal polytropic EOS ( $\Gamma = 2$ ), plus some sort of “perturbing agent.” The methods by which we drive a star to a non-equilibrium state involve: 1) giving the star an initially ingoing velocity profile, and 2) collapsing a spherical shell of scalar field onto it. Neither method can be considered truly perturbative since both can drive the star to total obliteration or prompt collapse to a black hole, but we use this term since a better one is lacking.

Sec. II provides the theory describing our systems and the numerical methods we use to simulate them. In Sec. IV, we begin our study of stellar collapse by extensively covering the parameter space of initial conditions for velocity-perturbed stars. The results from this section provide a broad view of the range of dynamical scenarios one can expect in the catastrophic collapse of NSs. We then employ this knowledge in our examination of the solutions that lie on the verge of black hole formation. Both Type I and Type II solutions are found. The stars’ Type I critical behavior is explored in Sec. V (their

Type II behavior has been investigated in a related paper [42]). The threshold solutions we calculate from the Type I study are then compared to unstable TOV solutions. In addition, for the first time, a parameter-space boundary separating the two types of phenomena is identified and discussed. Finally, we conclude in Sec. VI with some closing remarks and notes on possible future work.

## II. THEORETICAL MODEL

The equations and methods employed in this study closely follow those used in [42]. The primary difference is that we sometimes use a massless scalar field that is minimally coupled to gravity, and hence to the fluid. We refer the reader to [42] for details regarding the evolution of the hydrodynamics equations, but give here the equations that describe this “fluid+scalar” system and the methods used to evolve the scalar field.

### A. The Geometry Equations

We largely follow the notation established in our previous paper on Type II collapse of a perfect fluid [42]. We use geometrized units such that  $G = c = 1$ , and tensor notation and sign conventions that follow Wald [43]. When coordinate bases are explicitly used, Greek and Roman indices will refer to spacetime and purely spatial components, respectively (i.e.  $\mu, \nu, \dots \in \{0, 1, 2, 3\}$ , and  $i, j, k \in \{1, 2, 3\}$ ). Quantities in bold-face, e.g.  $\mathbf{q}, \mathbf{f}$ , are generally state vectors.

As in many previous critical phenomena studies in spherical symmetry [6, 18, 19, 22, 23], we employ the so-called polar-areal metric

$$ds^2 = -\alpha(r, t)^2 dt^2 + a(r, t)^2 dr^2 + r^2 d\Omega^2 \quad . \quad (3)$$

Since we will use a variety of sources in this study, we state the equations governing the metric functions using the formulation of Arnowitt, Deser and Misner (ADM) [44] and no specific assumption about the precise form of stress-energy tensor. To update  $a$  at each time step, we solve the Hamiltonian constraint,

$$\frac{a'}{a} = 4\pi r a^2 \varrho + \frac{1}{2r} (1 - a^2) \quad , \quad (4)$$

where  $\varrho$  is the local energy density measured by an observer moving orthonormal to the spacelike hypersurfaces. Note that a “prime” will denote differentiation with respect to  $r$  and a “dot” will represent differentiation with respect to  $t$ . In our coordinate basis, the 4-velocity,  $n^a$ , of this orthonormal observer has components

$$n^\mu = \left[ \frac{1}{\alpha}, 0, 0, 0 \right]^T \quad . \quad (5)$$

Hence,  $\varrho$  can be shown to be

$$\varrho = T_{\mu\nu} n^\mu n^\nu = T_{tt}/\alpha^2. \quad (6)$$

The lapse function  $\alpha$  is calculated at each step via the polar slicing condition,

$$\frac{\alpha'}{\alpha} = \frac{a'}{a} + \frac{1}{r} (a^2 - 1) - \frac{8\pi a^2}{r} \left[ T_{\theta\theta} - \frac{r^2}{2} (T^i_i - \varrho) \right]. \quad (7)$$

Even though it is used solely for diagnostic purposes, we state here for completeness the momentum constraint, which yields an evolution equation for  $a$ ,

$$\dot{a} = -4\pi r \alpha a j_r, \quad (8)$$

where  $j_r$  is the only non-vanishing component of the momentum density measured by the orthonormal observer,

$$j_a \equiv (g_{ac} + n_a n_c) n_b T^{bc}. \quad (9)$$

For diagnostic purposes, it is convenient to introduce the mass aspect function,  $m$ , given by

$$m(r, t) \equiv \frac{r}{2} \left( 1 - \frac{1}{a^2} \right). \quad (10)$$

We note that polar-areal coordinates *cannot* penetrate apparent horizons, but that the formation of a black hole in a given calculation is nonetheless signaled by  $2m(t, \tilde{r})/\tilde{r} \rightarrow 1$ , for some specific radial coordinate,  $r = \tilde{r}$ .

## B. The Matter Equations

We model NS matter as a perfect fluid. Modern conservative methods that utilize the characteristic structure of the fluid equations of motion expressed in *conservative* form have been very successful in evolving highly-relativistic flows in the presence of strong gravitational fields (see [38, 45–48] for a small but representative selection of papers on this topic), and we follow that approach here. In particular, we use a formulation used by Romero et al. [48] and a change of variables similar to that performed by Neilsen and Choptuik [47].

One way in which we drive NS models to collapse entails the inclusion of a massless scalar field which dynamically perturbs the star. We also use a driving mechanism that involves no scalar field. Not surprisingly, it turns out that the equations governing the geometry and fluid equations in the “fluid-only” system can be recovered from those in the “fluid+scalar” system simply by setting the scalar field,  $\phi(r, t)$ , to zero for all  $r$  and  $t$ . Hence, our numerical implementation always uses the full “fluid+scalar” equations for determining fluid and geometric fields: if we wish to include the scalar field, we simply initialize it to a non-zero value and evolve it in tandem with the fluid. Thus, by stating the fluid equations of motion (EOM) for the “fluid+scalar” system, we

are also simultaneously—yet indirectly—stating them in the “fluid-only” system.

The EOM for the two matter sources are derived, in part, from the local conservation of energy

$$\nabla_a T^a_b = 0, \quad (11)$$

where  $T_{ab}$  is the *total* stress-energy tensor. Since there is no explicit coupling between the two matter sources, the total stress tensor is a sum of the stress tensors of the individual sources

$$T_{ab} = \tilde{T}_{ab} + \hat{T}_{ab}, \quad (12)$$

where  $\hat{T}_{ab}$  and  $\tilde{T}_{ab}$  are the stress-energy tensors of the fluid and scalar field, respectively. Further, the local conservation of energy equation holds *separately* for each stress-energy. Specifically,

$$\nabla^a T_{ab} = \nabla^a \tilde{T}_{ab} = \nabla^a \hat{T}_{ab} = 0. \quad (13)$$

The scalar field stress-energy tensor is

$$\tilde{T}_{ab} = \nabla_a \phi \nabla_b \phi - \frac{1}{2} g_{ab} (\nabla_c \phi \nabla^c \phi + 2V(\phi)) \quad (14)$$

where  $V(\phi)$  is the scalar potential. In the following equations, we will assume that  $V(\phi)$  is non-zero, however, we have set  $V(\phi) \equiv 0$  in all of the calculations reported below. Since there is no direct interaction between the scalar field and the fluid, (13) yields the usual equation of motion for the scalar field:

$$\square \phi \equiv \nabla^a \nabla_a \phi = \partial_\phi V(\phi). \quad (15)$$

We can convert this to a system of first-order (in time) PDEs by introducing auxiliary variables,  $\Xi$  and  $\Upsilon$ , defined by

$$\Xi \equiv \phi' \quad , \quad \Upsilon \equiv \frac{a}{\alpha} \dot{\phi}. \quad (16)$$

With these definitions the EOM become

$$\dot{\Xi} = (X\Upsilon)' \quad , \quad (17)$$

$$\dot{\Upsilon} = \frac{1}{r^2} (r^2 X\Xi)' - \alpha a \partial_\phi V \quad , \quad (18)$$

where  $X \equiv \alpha/a$ .

The fluid equations of motion can be easily derived from the definition of the perfect fluid stress-energy tensor,

$$\hat{T}_{ab} = (\rho + P) u_a u_b + P g_{ab} \quad , \quad (19)$$

the local conservation of energy equation (13) and the *local conservation of baryon number*

$$\nabla_a (\rho_\circ u^a) = 0 \quad . \quad (20)$$

Here,  $u^a$  is the 4-velocity of a given fluid element,  $P$  is the isotropic pressure,  $\rho = \rho_\circ (1 + \epsilon)$  is the energy density,

$\rho_o$  is the rest-mass energy density, and  $\epsilon$  is the specific internal energy. Instead of the 4-velocity of the fluid, a more useful quantity is the radial component of the Eulerian velocity of the fluid as measured by a Eulerian observer:

$$v = \frac{au^r}{\alpha u^t} \quad , \quad (21)$$

where  $u^\mu = [u^t, u^r, 0, 0]$  (recall that we are working in spherical symmetry). The associated “Lorentz gamma function” is defined by

$$W = \alpha u^t \quad . \quad (22)$$

Given the fact that the 4-velocity is time-like and unit-normalized, i.e.  $u^\mu u_\mu = -1$ ,  $v$  and  $W$  are related by

$$W^2 = \frac{1}{1 - v^2} \quad . \quad (23)$$

In conservation form, the fluid’s EOM are

$$\partial_t \mathbf{q} + \frac{1}{r^2} \partial_r (r^2 X \mathbf{f}) = \boldsymbol{\psi} \quad , \quad (24)$$

where the state vector  $\mathbf{q}$  is a vector of *conserved* variables, and  $\mathbf{f}$  and  $\boldsymbol{\psi}$  are—respectively—the flux and source state vectors. Our choice of conserved variables follows that of Neilsen and Choptuik [47], and leads to improved accuracy in the ultrarelativistic regime ( $\rho \gg \rho_0$ ):

$$\mathbf{q} = \begin{bmatrix} D \\ \Pi \\ \Phi \end{bmatrix} \quad , \quad \mathbf{f} = \begin{bmatrix} Dv \\ v(\Pi + P) + P \\ v(\Phi + P) - P \end{bmatrix} \quad , \quad \boldsymbol{\psi} = \begin{bmatrix} 0 \\ \Sigma \\ -\Sigma \end{bmatrix} \quad , \quad (25)$$

where

$$D = a\rho_o W \quad , \quad (26)$$

$$\Pi = E - D + S \quad , \quad (27)$$

$$\Phi = E - D - S \quad , \quad (28)$$

$$S = \rho_o h W^2 v \quad , \quad (29)$$

$$E = \rho_o h W^2 - P \quad , \quad (30)$$

$h \equiv 1 + \epsilon + P/\rho_o$  is the the specific enthalpy of the fluid,  $D$  is the Eulerian rest-mass density, and  $\Pi$  and  $\Phi$  are linear combinations of the Eulerian momentum density ( $S$ ) and internal energy density ( $E - D$ ). We use  $P$ ,  $\rho_o$ , and  $v$  as primitive variables. For the sake of efficiency, we state the source function,  $\Sigma$ , in terms of derivatives of the metric functions so that additional matter sources can be incorporated into the model more easily:

$$\Sigma \equiv \Theta + \frac{2PX}{r} \quad (31)$$

and

$$\Theta = -\frac{2\dot{a}S}{a} - \frac{\alpha'}{\alpha} X E - \frac{a'}{a} X (Sv + P) \quad . \quad (32)$$

In practice, we use a simplified form of  $\Theta$  derived from the constraints (4,8) and the slicing condition (7) to eliminate  $a'$ ,  $\alpha'$  and  $\dot{a}$ . However, this requires knowledge of the full stress-energy tensor,  $T_{ab}$ , not just the fluid’s stress-energy tensor,  $\hat{T}_{ab}$ , to calculate. In the “fluid+scalar” system,

$$\begin{aligned} \Theta = & \alpha a \left\{ (Sv - E) \left[ 4\pi r (2P - V(\phi)) + \frac{m}{r^2} \right] \right. \\ & + P \left( \frac{m}{r^2} - 4\pi r V(\phi) \right) \Big\} \\ & - 2\pi r X \left[ 4\Xi \Upsilon S + (\Xi^2 + \Upsilon^2) (Sv + P + E) \right] \quad . \end{aligned} \quad (33)$$

When following the gravitational interaction between the fluid and scalar field, particularly interesting quantities to track are the two contributions to  $dm/dr$ :

$$\frac{dm}{dr} = 4\pi r^2 \varrho = 4\pi r^2 \varrho_{\text{fluid}} + 4\pi r^2 \varrho_{\text{scalar}} \quad , \quad (34)$$

$$\frac{dm_{\text{fluid}}}{dr} = 4\pi r^2 E \quad , \quad (35)$$

$$\frac{dm_{\text{scalar}}}{dr} = 4\pi r^2 \left[ \frac{1}{2a^2} (\Xi^2 + \Upsilon^2) + V(\phi) \right] \quad . \quad (36)$$

However, the two mass contributions can only be unambiguously differentiated in regions of non-overlapping support, since—for instance— $\partial m_{\text{scalar}}/\partial r$  depends on metric quantities which in turn depend on the local energy content of all matter distributions that are present. We note that expressing  $\frac{dm}{dr}$  in the form of Eq. (34) is possible because of our particular gauge choice.

The EOS closes the system of hydrodynamic equations. Because of the extensive nature of our parameter space survey, we wish to restrict ourselves to closed-form (i.e. non-tabulated) state equations. For isentropic flows, the polytropic EOS,

$$P = K \rho_o^\Gamma \quad , \quad (37)$$

for some constant,  $K$ , and adiabatic index,  $\Gamma$ , is commonly used. In addition, we use the “ideal-gas” or “gamma-law” EOS

$$P = (\Gamma - 1) \rho_o \epsilon \quad . \quad (38)$$

Our initial NS models are solutions to the spherically-symmetric hydrostatic Einstein equations, and are commonly known as Tolman-Oppenheimer-Volkoff (TOV) solutions [39, 41]. We use both EOSs (38,37) to set the initial data, but use only the ideal-gas EOS (38) to evolve any specific configuration [71]. To simulate stiff matter at super-nuclear densities—characteristic of neutron stars—we use  $\Gamma = 2$  in all of the calculations described below. We also note that, as pointed out by Cook et al. [49], the constant  $K$  can be thought of as the fundamental length scale of the system, with which one can use to scale any dynamical quantity with values of  $(K, \Gamma)$  to a system with different values  $(K', \Gamma')$ . As with  $G$  and  $c$ , we set  $K = 1$ .

This makes our equations unitless, ensuring that our dynamical variables are not at arbitrarily different orders of magnitude, and, as discussed in App. A, expediting the transformation of results to another set of  $(K, \Gamma)$ .

In summary, in our simulations of self-gravitating, ideal-gas fluids, the fluid is evolved by solving (24,25), the scalar field is evolved using (17-18), while the geometry is simultaneously calculated using the Hamiltonian constraint (4) and the slicing condition (7). The specific methods we employ to numerically integrate these equations are briefly explained in Sec. III.

### C. Initial Star Solutions

Since the TOV equations take the form of a coupled set of ODEs, their solution does not generally require the use of sophisticated numerical methods. Readers who are interested in more details are referred to the pseudo-code description in Shapiro and Teukolsky [50], as well as the discussion of our specific approach given in [51].

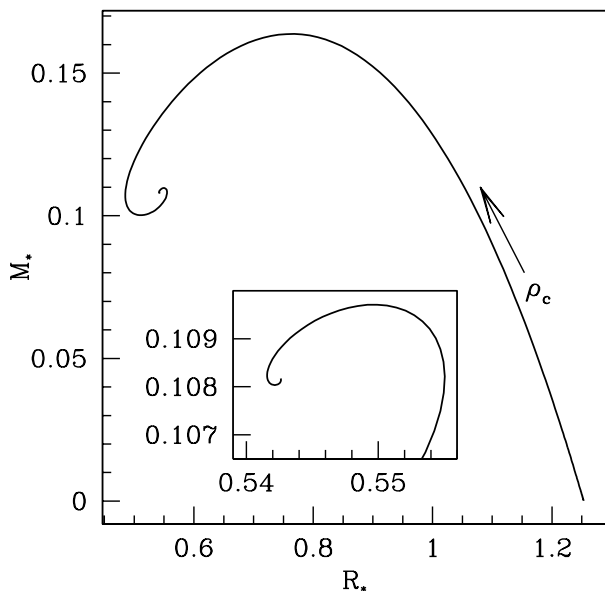


FIG. 1: Mass versus radius of TOV solutions using  $\Gamma = 2$  and  $K = 1$  with the polytropic EOS (37). In the inset, we show a detailed view of the spiraling behavior. The arrow along the right side of the curve indicates the direction of increasing central density.

Analysis of TOV solutions has a rich history [52] which we will not discuss here. We do, however, wish to note one important aspect of such solutions that is crucial to understanding their role in Type I critical behavior, and which has already been touched upon in the Introduction in the context of boson stars. Given an EOS, the TOV solutions can be parameterized by their central pressures; in our case, the EOS (37) allows us to reparameterize the solutions with respect to the central

rest-mass density,  $\rho_c$ . Arguments from linear stability analysis [52] tell us that TOV solutions with the smallest central densities are stable to small perturbations, while those solutions with  $\rho_c$  at the opposite end of the spectrum (large  $\rho_c$ ) are unstable. A plot of  $M_*(R_*)$  is shown in Fig. 1, where  $R_*$  is the radius of the star and we see that  $M_*(R_*)$  winds-up with increasing central density. At the global maximum of  $M_*(R_*)$  the fundamental, or lowest, mode becomes unstable. After each subsequent local extremum in the direction of increasing  $\rho_c$ , the next lowest mode becomes unstable. For instance, there are four local extrema of  $M_*(R_*)$  shown in Fig. 1, so those solutions with the largest  $\rho_c$  will have their four lowest modes exponentially grow in time.

As discussed previously, black hole critical solutions are typically characterized by a single growing mode. Hence, the Type I behavior associated with “perturbed” TOV solutions can be immediately anticipated to entail those TOV solutions that lie between the first and second extrema of  $M_*(\rho_c)$ . For subsequent reference we note that with the units and EOS that we have adopted, the most massive stable TOV solution has a central density  $\rho_c \simeq 0.318$  and a mass  $M_* \simeq 0.1637$ .

After the initial, star-like solution is calculated, an incoming velocity profile is sometimes added to drive the star to collapse. In order to do this, we follow the prescription used in [10] and [6]. The method described therein involves specifying the coordinate velocity,

$$U \equiv \frac{dr}{dt} = \frac{u^r}{u^t} \quad , \quad (39)$$

of the star, and then finding the Eulerian velocity,  $v$ , once the geometry has been calculated. In general, the profile takes the algebraic form

$$U(x) = A_0 (x^3 - B_0 x) \quad . \quad (40)$$

The two profiles that were used in [6] are

$$\begin{aligned} U_1(x) &= \frac{U_o}{2} (x^3 - 3x) \quad , \\ U_2(x) &= \frac{27 U_o}{10\sqrt{5}} \left( x^3 - \frac{5x}{3} \right) \quad , \end{aligned} \quad (41)$$

where  $x \equiv r/R_*$ . Unless stated otherwise,  $U_1$  will be used for all the results herein.

Specifying the coordinate velocity instead of  $v$  complicates the computation of the metric functions at  $t = 0$ . Our method for dealing with this difficulty is described in App. B.

### III. NUMERICAL TECHNIQUES

Simulating the highly-relativistic flows encountered in the driven collapse of NSs entails solving a system of coupled, partial and ordinary differential equations that describe how the fluid, scalar field, and gravitational field



evolve in time. High-resolution shock-capturing methods are used to evolve the fluid and the Iterative Crank Nicholson method, with second-order spatial differences, is used for the scalar field. Both methods are second-order accurate, except that the fluid method is first-order accurate near shocks and at local extrema. The Rapid Numerical Prototyping Language (RNPL) written by Marsa and Choptuik [53] is used to handle checkpointing, input/output, and memory management for all our simulations; we do not use the language of RNPL itself for our finite differencing, but use original, secondary routines that are called from the primary RNPL routines. More details of the code, along with descriptions of code tests can be found in [42, 51].

#### IV. VELOCITY-INDUCED NEUTRON STAR COLLAPSE

Here we present a description of the various dynamic scenarios we have seen in perturbed NS models, as a function of the initial star solution and the magnitude of the initial velocity profile. These results are compared to those from previous studies—most notably that of Novak [6]—but also provide some new insights. Specifically, this section provides a description of various phases we have identified in parameter space, including those from a survey of the subcritical regime that is more detailed than has been reported in prior work. In Sec. V we then focus on the critical phenomena observed at the threshold of black hole formation, and where collapse is induced via interaction of the fluid star with a collapsing pulse of massless scalar field.

In this section any specific TOV solution is driven out of equilibrium by endowing it with an ingoing profile for the initial coordinate velocity,  $U(r, 0)$ , as described in Sec. II C. We measure the magnitude of this perturbation by the absolute value of the minimum value of the Eulerian velocity  $v$ ,  $v_{\min}$ , at the initial time. We find that  $v_{\min}$  is uniquely specified by the parameter  $U_0$  provided that we follow the prescription for generating perturbed TOV stars given in App. B. We also note that  $v_{\min}$  is a more physical quantity than similar parameters—e.g.  $U_0$ —that pertain to the fluid’s gauge-dependent, coordinate velocity.

Our survey used 22 different stable TOV solutions—specified by the initial central density  $\rho_c$ —shown in Fig. 2. The solutions used for the parameter space survey are displayed along the  $M_*(\rho_c)$  curve for  $\Gamma = 2$  TOV solutions. We note that a wide spectrum of stars were chosen, from non-compact stars that are relatively large and diffuse, to compact and dense stars.

By sampling  $v_{\min}$  and the initial central density of the star,  $\rho_c$ , we have created a type of “phase diagram” for the various ways in which perturbed TOV solutions evolve. The phase diagram is shown in Fig. 3. We sample the parameter space by varying the parameter  $v_{\min}$  for each value of  $\rho_c$ . Approximately 360  $\{\rho_c, v_{\min}\}$  sets were

run in order to resolve the phase boundaries. Given any combination of the central value of the star’s rest-mass density,  $\rho_c$ , and  $v_{\min}$ , the system will evolve in a fashion specified by the diagram. In Fig. 4, we display the phases in  $(M_*, v_{\min})$  space.

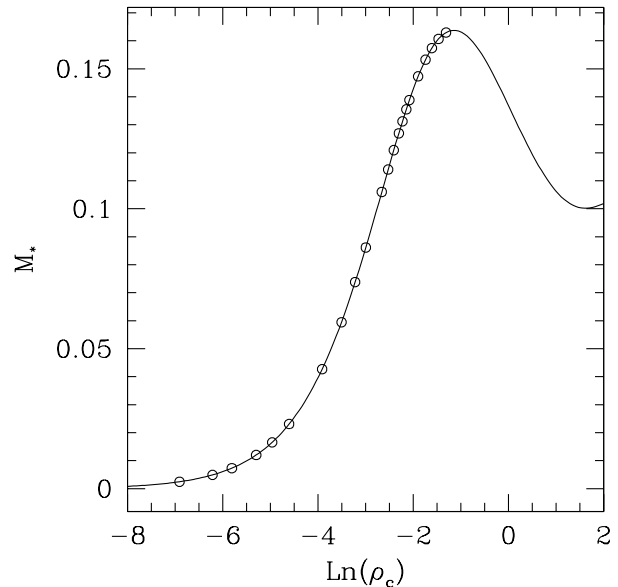


FIG. 2: Initial TOV solutions used in the parameter space survey.

The types of dynamical outcomes or “phases” identified in Figs. 3–4 are:

**Prompt Collapse (PC):** The initial “perturbation” is so strong that the star is driven directly to black hole formation. The fluid collapses homologously—or uniformly—and insignificant amounts of material are ejected before the black hole forms.

**Shock-Bounce-Collapse (SBC):** The perturbation is not sufficient to spontaneously form a black hole, but is strong enough to eventually drive the star to collapse. The outer part of the star collapses at a faster rate than the interior and eventually bounces off the denser core, producing an outgoing shock which expels a significant portion of the outer layers of the star.

**Shock-Bounce-Dispersion (SBD):** This case is quite similar to the SBC scenario, except a black hole never forms. Instead, the star contracts until it reaches some maximum density and pressure at the origin which is great enough to expel the remainder of the star, leaving behind an ever-decreasing amount of matter. This final explosion results in another outgoing shock wave that typically overtakes and engulfs the first shock.

**Shock-Bounce-Oscillation (SBO):** As the perturbation is decreased, the rebound of the interior no

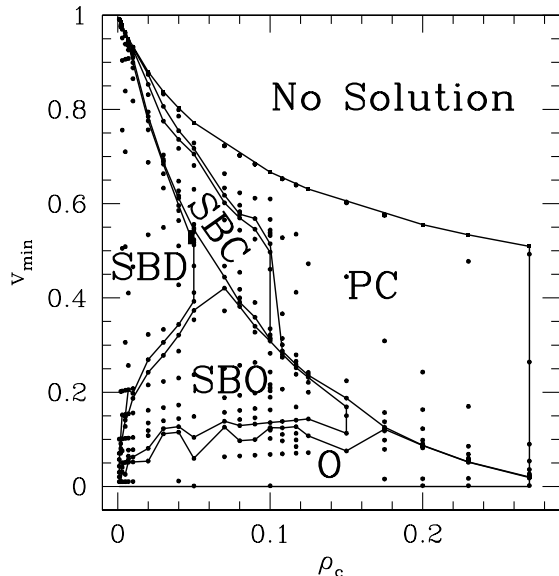


FIG. 3: Parameter space showing the regions in which various outcomes (phases) occur. The space is spanned by the initial magnitude of the velocity perturbation,  $v_{\min}$ , and the initial central density of the star,  $\rho_c$ . The small black rectangular region located at  $(\rho_c, v_{\min}) \sim (0.05, 0.53 - 0.55)$  represents a set of solutions that undergo an SBO-type evolution. Phase Legend: PC = Prompt Collapse, SBC = Shock-Bounce-Collapse, SBD = Shock-Bounce-Dispersal, SBO = Shock-Bounce-Oscillation, O = Oscillation. See text for further explanation of the various phases.

longer results in complete mass expulsion. Rather, some matter remains after the first two shocks propagate outwards and this matter settles into a new equilibrium state by oscillating away any excess kinetic energy via shock-heating. After the oscillations dampen away, a star is left behind that is larger, sparser and hotter than the original.

**Oscillation (O):** Finally, if the inward velocity is minimal, then the perturbed star will undergo adiabatic oscillations at its fundamental frequency and overtones with a negligible expulsion of mass.

Quantitative definitions and further descriptions of these end states can be found in App. C.

The phase boundaries—with the possible exception of that between the SBO/O states—appear to be quite smooth. This uniformity lends itself to global characterizations, such as a comparison of the dynamical scenarios possible between less compact stars (low  $\rho_c$ ) and more compact stars (high  $\rho_c$ ). For example, we find that only low  $\rho_c$  stars can undergo a complete explosion that disperses the star’s matter to infinity, and they require significantly larger perturbations to form black holes. Both of these aspects are intuitive since such stars generate less spacetime curvature. On the other hand, more compact stars induce greater spacetime curvature, and so

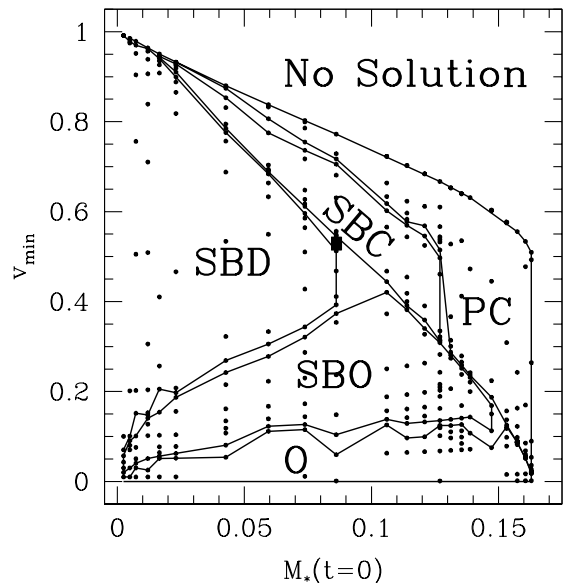


FIG. 4: Parameter space showing the regions in which various outcomes occur. This is the same data shown in Fig. 3 but displayed with respect to the initial magnitude of the velocity perturbation,  $v_{\min}$ , and the initial mass of the star,  $M_*(0)$ . Note that  $M_*$  is the gravitational mass of the *static* star solution and not of the perturbed star. Since  $M_*(\rho_c)$  is monotonic in the region we sampled (Fig. 2), this figure is essentially a distortion of Fig. 3. The most massive stars shown here have  $\rho_c = 0.27$  and  $M_* = 0.1629$ . The small black rectangular region located at  $(M_*, v_{\min}) \simeq (0.086, 0.53 - 0.55)$  represents a set of solutions that undergo an SBO-type evolution. See Fig. 3 caption and text for definition of various phases that are identified.

are more difficult—and apparently impossible in some cases—to completely disperse from the origin.

From our survey, we have also found that it is not possible to drive some of the less compact stars to black hole formation, regardless of the size of the initial velocity perturbation. Black holes arise through SBC dynamical scenarios for  $\rho_c \gtrsim 0.007$ , and homologous collapse to a black hole (PC) only occurs for stars with  $\rho_c \gtrsim 0.01$ . Since we observe Type II critical phenomena for  $0.01 \lesssim \rho_c \lesssim 0.05343$  (see [42] for more details), we surmise that arbitrarily small black holes can form for this entire range of TOV solutions. For  $\rho_c \gtrsim 0.05344$ , we find that the threshold solutions are Type I solutions, suggesting the smallest black holes that can evolve from such stars have finite masses. The Type I behavior seen in perturbed stars will be discussed in Sec. V.

In order to compare our results to Novak’s, we need to transform our scale to his. However, it is unclear what scale Novak used. He stated masses in terms of solar masses, but wrote “ $K = 0.1$ ” without specifying the units of  $K$ . This possibly suggests that he used geometrized units in that case. Given this uncertainty, we attempt to compare our values to his by determining the  $K$  that

makes the mass of our last stable TOV solution (i.e. the solution with the maximum mass) correspond to his value of  $3.16M_\odot$ . We will place a “hat” over all quantities that we state in these units. Using the methods described in App. A, we find that this factor of  $K$  is  $\hat{K} = 5.42 \times 10^5 \text{cm}^5 \text{g}^{-1} \text{s}^{-2}$ . Let  $M_1$  be the mass of the least massive star that can form a black hole through any scenario, and  $M_2$  be the mass of the least massive star that we observe to undergo prompt collapse to a black hole. In our units, we find  $M_1 \simeq 0.01656$  at  $\rho_c = 0.007$ , and  $M_2 \simeq 0.02309$  at  $\rho_c = 0.01$ . Using  $\hat{K}$  to convert our masses to his yields  $\hat{M}_1 = 0.320M_\odot$  versus  $\hat{M}_1 = 1.155M_\odot$ , and  $\hat{M}_2 = 0.446M_\odot$  where Novak reports  $\hat{M}_2 \approx 2.3M_\odot$ . Note that  $\hat{M}_2$  is estimated from Fig. 5 of [6], where a velocity profile equivalent to our  $U_2$  profile (41) is used. Since we have only performed the parameter space survey for  $U_1$  we cannot say what we would get for  $M_2$  when using  $U_2$ . However, Novak performed a comparison between these two profiles and found that his estimates for  $M_1$  deviated by about 1% between the two. Hence, we believe it is adequate to quote his result for  $U_2$  in order to compare to our result for  $U_1$ .

The difference in masses is also obvious in our respective phase diagrams from the parameter space surveys, where the point along the  $\rho_c$  axis ( $n_B$  in Novak’s case) at which black holes can form occurs for noticeably more compact stars in Novak’s case [72]. Another significant distinction we see in our phase space plot is an absence of SBC states for larger  $\rho_c$ . Novak seems to observe such scenarios all the way to the turnover point ( $\rho_c = 0.318$ ), whereas we find that they no longer happen for  $\rho_c \gtrsim 0.108$ .

Additionally, we believe our study is the first to extensively cover the subcritical region of NS collapse. While the method by which the NSs are perturbed may not be the most physically relevant prescription, we are able to see all the collapse scenarios found in previous works. Much of the previous research focused on compact stars near the turnover point or studied some other region exclusively (e.g. [36], [54], [48], [38], [37]), while others individually observed much of the phenomenon without thoroughly scrutinizing the boundaries between the phases ([7], [6], [10]).

Our parameter space survey also sheds light on the critical behavior observed at the threshold of black hole formation. Specifically, we see that the SBD/SBO boundary on the subcritical side of the diagram seems to be correlated with the transition from Type II to Type I critical behavior. The Type II threshold lies along the SBD/SBC boundary, while the Type I threshold occurs along the line that separates SBO and O cases from black hole-forming cases. We have been able to determine that  $\rho_c \approx 0.05344$  is the approximate point at which the transition from Type II to Type I behavior occurs. For Type II minimally subcritical solutions near this transition, the matter disperses from the origin but it is difficult to say if it escapes to infinity since our grid refinement procedure is incapable of coarsening the domain. Conse-

quently, the time step is too small to allow for longtime evolutions of these dispersal cases, and we are unable to guarantee that they do indeed disperse to infinity. In addition, the self-similar portion of these marginally subcritical solutions entails only a small amount of the original star’s matter, the remainder of which could, in principle, collapse into a black hole at a time after the inner self-similar component departs from the origin. Hence, with our current code, it is difficult to determine the ultimate fate of these dispersal scenarios.

What does this parameter survey suggest about the black hole mass function from driven NS collapse? For PC scenarios, the black hole mass is approximately the same as the progenitor star’s mass. The SBC/PC boundary marks where the black hole mass function can begin to significantly deviate from the stellar mass function. The least extreme (smallest  $v_{\min}$ ) SBC scenario takes place near  $v_{\min} \simeq 0.3$ ,  $\rho_c \simeq 0.1$  and  $M_\star \simeq 0.13$ . Such a large velocity profile may seem unphysical, however, a self-consistent, general relativistic simulation of a core collapse supernova in spherical symmetry performed by Liebendörfer et al. [55] led to a minimum velocity of  $\sim -0.6c$  soon after bounce. This suggests that  $v_{\min} \gtrsim 0.3$  is not so unrealistic. Also, it means that Type II behavior may be physically attainable in nature if—in fact— $v_{\min}$  reaches the magnitudes seen in [55] since  $v_{\min} \simeq 0.55$  is the smallest velocity profile that leads to Type II behavior. However, we find that  $M_{\text{BH}}$  becomes a power-law only when  $v_{\min}$  has been tuned to less than 0.01% of the critical value [42], suggesting that such cases will not affect the black hole mass function significantly. Unfortunately, we have not measured the dependence of  $M_{\text{BH}}$  on  $v_{\min}$  and  $\rho_c$  in the SBC regime, and—therefore—are not sure if the distribution is non-trivial. We hope to measure this in the future.

Wan et al. [64] present a similar phase space survey of a head-on collision between two identical Gaussian distributions of stiff matter ( $\Gamma = 2$ ) to approximate the head-on merger of identical neutron stars. The two Gaussian distributions were boosted toward each other with the same velocity magnitude. The amplitude of the boost velocities and the initial central densities of the Gaussian distributions were varied to explore the nature of the critical surface. As the central densities were varied, the total baryonic masses of the pulses were kept constant by adjusting the width of each distribution. Like us, they find that there is a line that separates black hole forming initial conditions from NS forming conditions. Unlike our results, however, they find that their line is concave leftward, suggesting that there is a maximum density beyond which black hole formation is impossible independent of boost velocity. Further, it suggests that at a given initial central density (below this upper limit) there are two critical transitions: from NS-forming to BH-forming to NS-forming—i.e. there is a velocity value above which only NS formation is possible. Wan [66] explains further that the second threshold arises because at this point the merger produces a shock that heats the

gas to the point that collapse is prevented. In our system, black hole formation is always possible except for the sparsest stars.

## V. TYPE I CRITICAL PHENOMENA

In this section we describe the Type-I behavior observed when perturbing a TOV solution with an imploding pulse of scalar field. Please see [42] for a description of the Type II phenomena.

### A. Model Description

As others have done [28, 37], we use a minimally-coupled, massless scalar field to perturb our star solutions dynamically. The scalar field is advantageous for several reasons. First, the fact that the two matter models are both minimally-coupled to gravity with no explicit interaction between the two ensures that any resulting dynamics from the perturbation is entirely due to their gravitational interaction. Second, the EOM of the scalar field are straightforward to solve numerically and provide little overhead to the hydrodynamic simulation. Third, since gravitational waves cannot exist in spherical symmetry and the scalar field only couples to the fluid through gravity, it can serve as a plausible first approximation to gravitational radiation acting on these spherical stars.

We will continue to approximate NSs as polytropic solutions of the TOV equations with  $\Gamma = 2$ , and the factor in the polytropic EOS (37) will still be set to  $K = 1$  to keep the system unitless. Since all stellar radii  $R_\star$  satisfy  $R_\star < 1.3$  for such solutions, we will—by default—position the initial scalar field pulse at  $r = 5$ . This has been found to be well outside any star's extent and so ensures that the two matter sources are not initially interacting.

### B. The Critical Solutions

The evolution of the star towards the critical solution and the critical solutions themselves will be described in this section. As the scalar field pulse travels into the star, the star undergoes a compression phase wherein the exterior implodes at a faster rate than the interior. This is reminiscent of the velocity-induced shock-bounce scenarios described in Sec. IV. If the perturbation is weak, then the star will undergo oscillations with its fundamental frequency after the scalar field disperses through the origin and finally escapes to null infinity (higher harmonics are also excited). On the other hand, when the initial scalar shell is of sufficiently large amplitude, the star can be driven to prompt collapse, trapping some of the scalar field along with the entire star in a black

hole. Somewhere in between, the scalar field can compactify the star to a nearly static state that resembles an unstable TOV solution of slightly increased mass. The length of time the perturbed star emulates the unstable solution, which we will call the *lifetime*, increases as the initial pulse's amplitude is adjusted closer to the critical value,  $p^*$ . It is expected from this scaling behavior that a perfectly constructed scalar field pulse with  $p = p^*$  would perturb the star in such a way that it would resemble the unstable solution forever. This putative, infinitely long-lived state is referred to as the critical solution of the progenitor star.

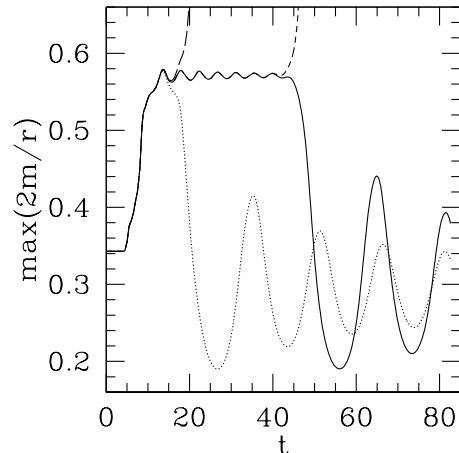


FIG. 5: Evolutions of  $\max(2m/r)$  from 4 solutions near the critical threshold of a star parameterized by  $\Gamma = 2$ ,  $\rho_c = 0.15$ . Shown are solutions far from threshold on the supercritical side (long dashes), near threshold on the supercritical side (short dashes), near threshold on the subcritical side (solid curve), and far from threshold on the subcritical side (dots). The two solutions near the threshold have been tuned to within machine precision of the critical value.

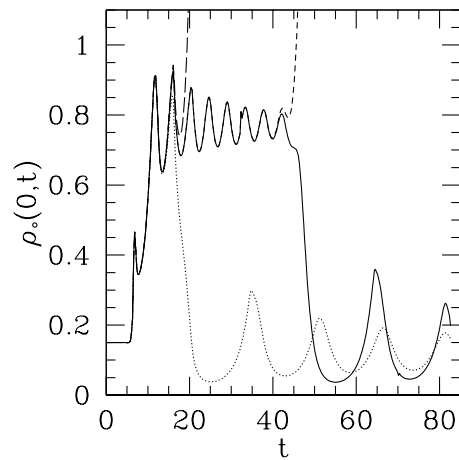


FIG. 6: Same as in Fig. 5 but of  $\rho_o(r=0, t)$ .

Examples of solutions near and far from the critical solution are illustrated in Figs. 5–6 for a star with

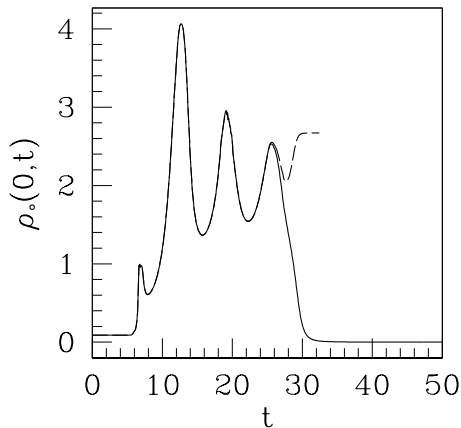


FIG. 7: Sample evolutions of the central rest-mass density for supercritical (dashes) and subcritical (solid) solutions from a progenitor star with  $\rho_c = 0.09$ . The solutions have been tuned to within machine precision of criticality. Note that  $\rho_o(0,t)$  for the supercritical calculation tends to a constant value since the “collapse of the lapse” has effectively frozen the star’s evolution near the origin. The subcritical solution evolves to an oscillating star that is larger and sparser than the original state; these oscillations are not visible at the scale used here.

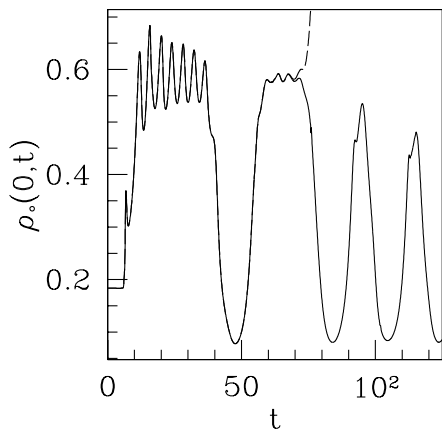


FIG. 8: Sample evolutions of the central rest-mass density for supercritical (dashes) and subcritical (solid) solutions from a progenitor star with  $\rho_c = 0.1835$ . The  $\rho_c = 0.1835$  star is the star with the smallest initial central density whose nearest-to-critical solution exhibits a momentary departure from the unstable equilibrium solution; this is indicated by the break between the two “plateaus” in the graph. This behavior is seen for most stars above  $\rho_c = 0.1835$ .

$\rho_c = 0.14$ . Here we show the evolution of the spatial maximum of  $2m/r$ ,  $\max(2m/r)$ , and the central density of the star for a series of solutions. The quantity  $2m/r$  is, effectively, a measure of the degree of compactification; the global maximum that  $2m/r$  can attain for the static TOV solutions studied herein is approximately 0.61, and  $2m/r \rightarrow 1$  when a black hole would form. The super-

critical systems far from the threshold quickly collapse to black holes as indicated here by the divergence of the central density and compactification factor. On the opposite side of the spectrum, we see that subcritical solutions undergo a series of oscillations. The plateau shown in the plots represents the period of time during which the marginally subcritical and supercritical solutions resemble the critical solution. We will see shortly that this critical solution is actually a star-like configuration oscillating about an unstable TOV solution. Interestingly, we do not see the secular growth in the central density with respect to time in these near-threshold solutions that others report [68]; these authors note that it is likely due to their use of a multi-dimensional code and lower effective resolution.

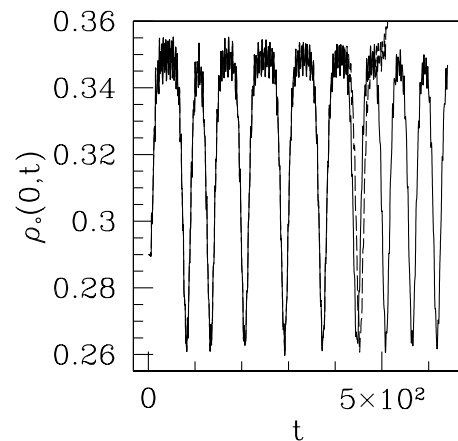


FIG. 9: Sample evolutions of the central rest-mass density for supercritical (dashes) and subcritical (solid) solutions from a progenitor star with  $\rho_c = 0.29$ . The supercritical solution undergoes a curious sequence not seen in many cases: after it deviates from the subcritical solution—instead of collapsing to a black hole immediately—it returns to it one last time before collapsing.

Instead of dispersing to spatial infinity as do the solitonic oscillon stars of [27], the marginally-subcritical TOV stars ultimately settle into bound states. Depending on the magnitude of  $p^*$  for a particular progenitor star, the final star solution will either be larger and sparser than the original (large  $p^*$ ), or it will oscillate indefinitely about the original solution. In reality, the star will radiate away the kinetic energy of the oscillation via some viscous mechanism. In our model, however, the only dissipation is the trivial amount from the numerical scheme, and that from the star shock-heating its atmosphere—transferring the kinetic energy of the bulk flow into internal energy. If the subcritical star settles to a sparser solution, it will do this through a series of violent, highly-damped oscillations similar to the SBO scenarios of velocity-perturbed stars described in Sec. IV. Examples of such subcritical SBO solutions are depicted in Figs. 5–7. The damped oscillations are best illustrated in the marginally subcritical solutions shown

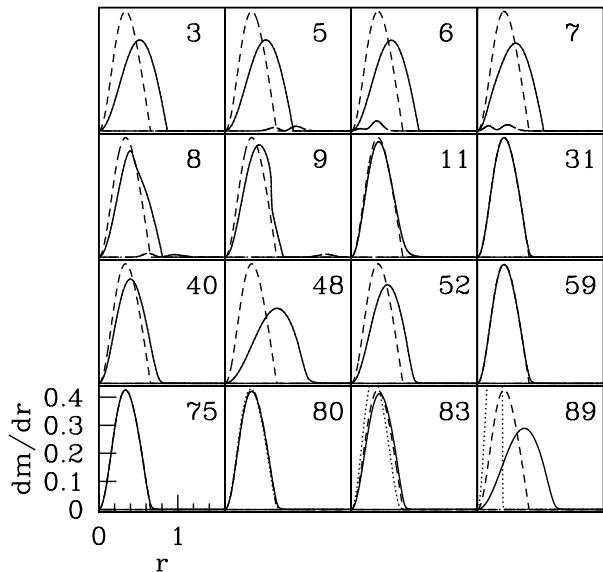


FIG. 10: Time series of fluid and scalar field contributions to  $dm/dr$  for the solutions closest to the critical threshold of progenitor stars with  $\rho_c = 0.197$ . The supercritical (subcritical) fluid contribution is the dotted (solid) curve, and the scalar field contribution that gives rise to the supercritical (subcritical) solution is shown as a dot-dashed (long-dashed) curve near the bottom of each frame (and is most visible in the third and fourth frames). The  $dm/dr$  of the fluid’s unstable, equilibrium solution that most closely approximates our critical solution is shown as the dashed line. The elapsed proper time measured at spatial infinity of each frame is shown in the upper-right corner. Since the differences between the supercritical and subcritical scalar field perturbations is on the order of machine precision, the subcritical scalar field contribution is completely obscured by the supercritical one. Also, the supercritical and subcritical fluid contributions are nearly identical until  $t = 80$ , when the two solutions begin to diverge from the critical solution.

in Figs. 5–6, since the oscillations of the subcritical solution of  $\rho_c = 0.09$  (Fig. 7) occur at an imperceptible scale.

For these sparser stars, the perturbation required to generate near-critical evolution is quite large and, consequently, is such that it drives the star to significantly *overshoot* the unstable TOV solution, setting it to ring about the unstable solution instead. This metastable ringing decreases with decreasing  $p^*(\rho_c)$ , or increasing  $\rho_c$ . For instance, the critical solution of the  $\rho_c = 0.09$  star seems to correspond to an unstable TOV star with central density  $\rho_c^* \simeq 2$  that oscillates such that  $0 < \rho_o(0, t) < 4$ . The increase in central density—from the initial stable star to the unstable star solution—represents an increase by a factor of 22. This is to be contrasted with the critical solution for the  $\rho_c = 0.29$  star which has a central density  $\rho_c^* \simeq 0.35$ —an increase by a factor of 1.2; this critical solution oscillates such that  $0.32 < \rho_o(0, t) < 0.38$ . This trend will be discussed further in Sec. V C.

In addition to smaller oscillations about the metastable states for denser initial stars, we see from Figs. 8–9 that near-critical evolutions can momentarily depart from their metastable states. The departures are illustrated by a break in the plateaus of the  $\rho_o(0, t)$  distributions. As  $\rho_c$  increases and gets closer to the turnover point, which is located at  $\rho_c = 0.318$ , we see that the number of distinct plateaus increases. The  $\rho_c = 0.1835$  solution is the smallest initial central density where two plateaus are observed, and  $\rho_c = 0.21$  is the first one where three are seen. For higher densities we see an ever-increasing number of plateaus, most likely because the difference between the progenitor solution and its corresponding critical solution diminishes. We explore possible causes of these departures in App. D.

As we can see in the time sequence of the scalar field and fluid contributions to  $dm/dr$  in Fig. 10, the marginally subcritical and supercritical stars leave the unstable TOV star configuration only to return to it after one oscillation about the progenitor solution. The unstable star solution shown was found by calculating a TOV solution with central density equal to the time average of  $\rho_o(0, t)$  of the solution tuned nearest to the threshold. The shock from the outer layers of the star reacting first to the increase in curvature is first seen at  $t = 9$  of this figure.

Making a quantitative comparison of the critical solution to an unstable star is not easy since the critical solution is not exactly static. If we make the assumption that the oscillation is sinusoidal, we can take a time-average of the solution when it most resembles an unstable star. We first start with the subcritical solution that is closest to the threshold. The periods over which the solution best approximates the unstable solution are determined by qualitatively judging where the sequences of quasi-normal oscillations begin and end. The central density,  $\rho_c^*$ , of the critical solution is then estimated as the time-average of  $\rho_o(0, t)$  over each of these periods. For each system with multiple periods (or plateaus) studied here, we have found the plateau averages all agree with each other to within their standard deviation. Hence, we feel that this is a consistent method for identifying the unstable star associated with a critical solution.

After identifying a perturbed star’s associated metastable solution, we can compare its shape with the solution it oscillates about during a plateau. To perform this comparison for  $\rho_c = 0.197$ , we used the time-average of the perturbed star during the second plateau and the TOV solution with central density  $\rho_c^*$ . The results of this comparison are shown in Figs. 11–12, where metric and fluid functions from the time-average and the estimated unstable TOV solution are shown together along with their differences. These figures clearly show that, during “plateau epochs”, the critical solution closely approximates an unstable TOV solution of similar central density. The relative deviation between the two solutions increases near the radius of the star,  $R_*$ , which is not surprising since the fluid’s time-averaged velocity is

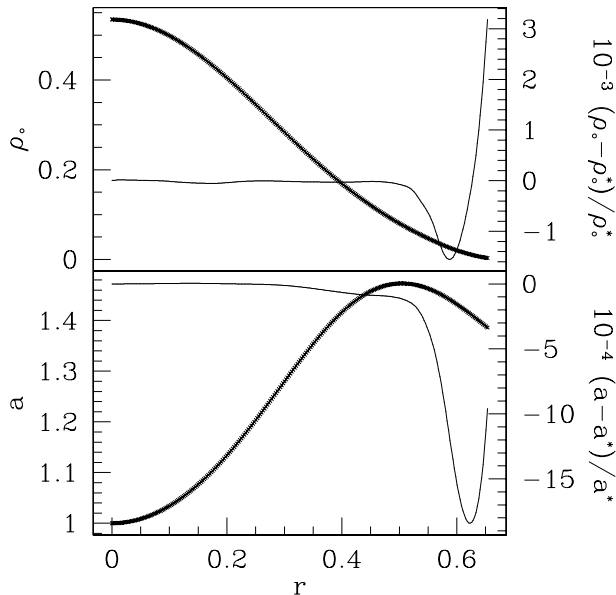


FIG. 11: Time-averages ( $\times$ 's) of  $\rho_o$  (top) and  $a$  (bottom) from the marginally subcritical solution compared to those from the associated unstable TOV solution ( $\rho_o^*$  and  $a^*$ , dark solid curves) it best approximates. The subcritical solution used has been tuned to within machine precision of the critical solution, and whose initial star has central density of  $\rho_c = 0.197$ . Only every eighth point of the time-averaged distributions is displayed. Also shown (light solid curves) are the relative differences between these two sets of functions. The curves are truncated at the stellar radius of the critical solution.

greatest there. Also, near  $R_*$  the star is most likely interacting with the atmosphere in a non-trivial way, which could alter its form near the surface. In fact, a similar discrepancy was observed in the critical boson star solutions in [28]; they found that the critical solutions had a longer “tail” than their corresponding static solutions. Still, the differences we see here are encouraging, and suggest strongly that the critical solutions we obtain are perturbed stellar solutions from the unstable branch.

### C. Mass Transfer and the Transition to the Unstable Branch

Not only does the perturbing scalar field momentarily increase the spacetime curvature near the origin as it implodes through the star, the gravitational interaction of the two matter fields involves an exchange of mass from the scalar field to the star. In Fig. 13, we provide a more explicit illustration of the mass exchange for two marginally subcritical solutions of stars with  $\rho_c = 0.197$  and  $\rho_c = 0.09$ . The total gravitating mass  $M_{\text{total}}$  is calculated via Eq. (10), while  $M_{\text{fluid}}$  ( $M_{\text{scalar}}$ ) is found by integrating  $dm_{\text{fluid}}/dr$  ( $dm_{\text{scalar}}/dr$ ) from the origin to the outer boundary. For each case, the non-trivial gravitational interaction of the fluid and scalar field can be rec-

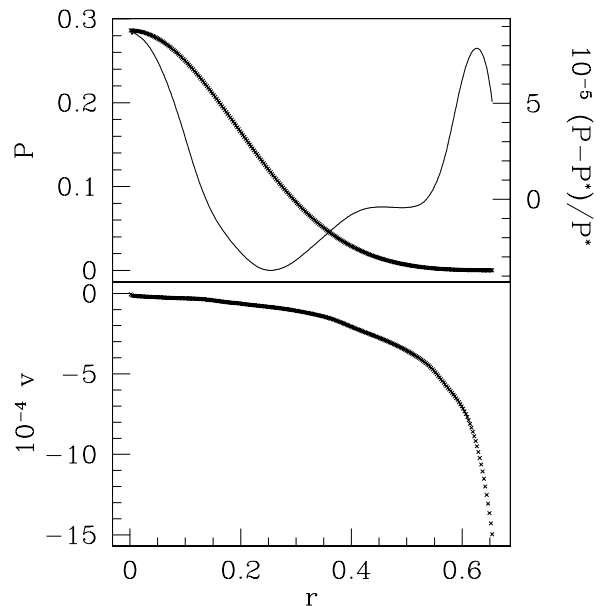


FIG. 12: Same as in Fig. 11 but for the functions  $P$  (top) and  $v$  (bottom).

ognized by the sudden change in their integrated masses, which occurs near  $t = 7$  in each plot. The perturbation for the  $\rho_c = 0.197$  star is small and does not transfer a significant portion of its mass to the star, whereas the perturbation required to drive the  $\rho_c = 0.09$  star to its marginally subcritical state transfers more than a third of its mass to the star. This dramatic interaction drives the star to oscillate wildly about its unstable counterpart—as seen in Fig. 7—and it eventually expels a great deal of the star’s mass as it departs from this highly energetic, yet unstable, bound state. The loss of the ejected matter from the grid is clearly seen in Fig. 13 as the long tail of  $M_{\text{fluid}}(t)$ , which begins to decrease well after the scalar field leaves the grid.

To examine how the amount of mass exchange varies for different critical solutions and to see where exactly critical solutions fall on the  $M_*$  versus  $\rho_c$  graph of equilibrium solutions, we constructed Fig. 14. The initial star solutions are indicated here on the left side—the stable branch—while their critical solutions are shown on the right along the unstable branch. There are two associated masses for each critical solution: the mass it would have if its profile exactly matched the unstable TOV solution with the same time-averaged central density, and its true mass. Both of these masses are indicated in Fig. 14 to the right of the turnover point. We find that the total fluid mass is always larger than its initial mass, whereas the mass of the attractor solution is always *smaller* than its stable progenitor. In addition, as the turnover is approached, both of these deviations diminish until, at turnover, the final mass of the fluid distribution corresponds to its initial mass *and* the mass of the unstable TOV solution.

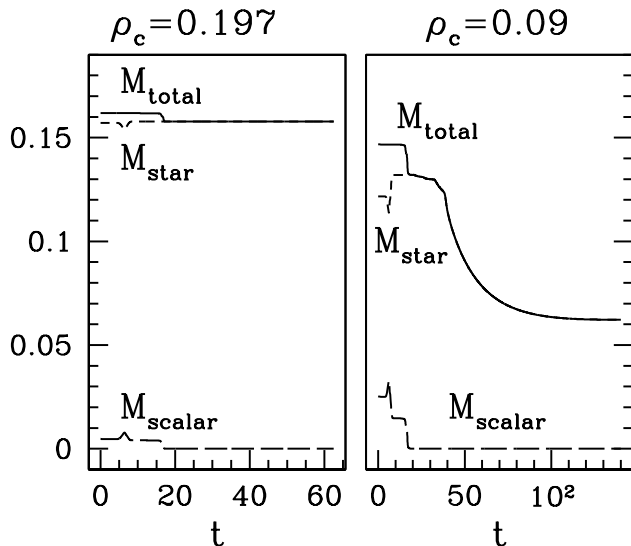


FIG. 13: Integrated masses of the matter fields as a function of time for marginally subcritical solutions of progenitor stars with  $\rho_c = 0.197$  (left) and  $\rho_c = 0.09$  (right). The decrease in  $M_{\text{total}}$  (solid curve) at the same time as  $M_{\text{scalar}}$  (long dashes) vanishes signifies the scalar field leaving the numerical grid; from the time it leaves,  $M_{\text{total}}$  is equivalent to  $M_{\text{fluid}}$  (short dashes).

The observed trend that the mass of the unstable TOV solution is always smaller than the progenitor's may be explainable in a number of ways. First, the assumption that the oscillations of the critical solution about the attractor solution are sinusoidal would most likely result in overestimates of  $\rho_c$  since the oscillations seem to decay in a nonlinear fashion over time. A larger  $\rho_c$  would then lead to a mass estimate smaller than it should be, since  $dM_*/d\rho_c < 0$  on the unstable branch. Second, it was seen in Figs. 7–9 that the oscillations of the critical solutions decrease with increasing  $\rho_c$ . The decrease in the amount of energy in these kinetic modes seems to be correlated with the decrease in the exchanged mass. A large portion of the exchanged mass must therefore go into the unstable star's kinetic energy.

#### D. Type I Scaling Behavior

As the amplitude of the initial pulse of scalar field is adjusted toward  $p^*$ , the lifetime of the metastable, near-critical configuration increases. To quantify the scaling for a given initial star solution, the subcritical solution closest to the critical one is first determined. This is done by tuning the amplitude of the scalar field pulse,  $p$ , until consecutive bisections yield a change in  $p$  smaller than machine precision. Let  $p^{\text{lo}}$  be the value of  $p$  that yields

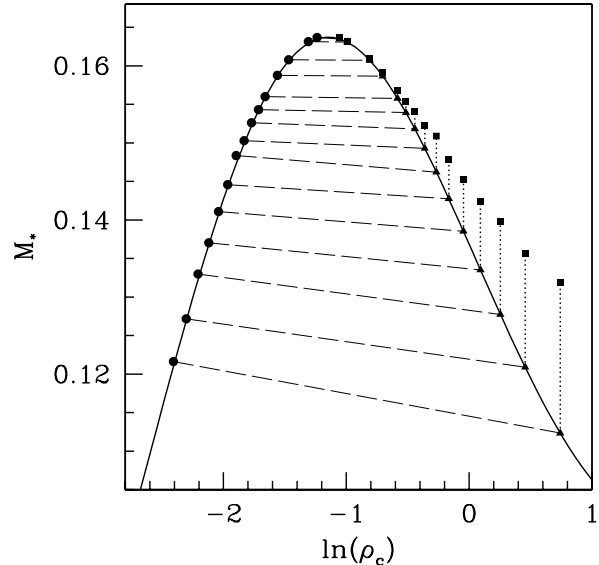


FIG. 14: Mass versus the log of the central density for equilibrium solutions (solid curve), a few of the initial data sets used (circles), and the critical solutions obtained from these initial data sets (triangles and squares). The central density of a critical solution was obtained by taking a time average of the central density when the star most resembled the attractor solution. The triangles show where these central densities lie on the unstable branch, and the mass denoted by a circle or square is of all the fluid in the numerical domain. The dashed and dotted lines indicate the solutions' associations.

the subcritical solution that most closely approximates the critical solution. For each  $p$ , a unique solution is produced that resembles this marginally subcritical solution for different lengths of time, determined by how close  $p$  is to  $p^*$ . Assuming that the  $p^{\text{lo}}$  solution resembles the critical solution longer than any other, the lifetime,  $T_0(p)$ , is then the proper time measured at the origin that elapses until  $\max(2m/r)$  deviates from that of the  $p^{\text{lo}}$  solution by more than 1%. These lifetimes  $T_0(p)$  are then fit against the expected trend (2). An example of such a fit is given in Fig. 15. Since supercritical solutions resemble the critical solution as well as subcritical solutions, both kinds can be used when determining the scaling exponent  $\sigma$ . The exponent is the negative of the slope of the fitted line. The deviation of the code-generated data from the best-fit has an obvious modulation, which may be due to the periodic nature of the near-threshold solutions. Similar modulations in the scaling behavior have also been reported for the case of head-on neutron star collisions [69]. In addition, we note that the values of  $\sigma(\rho_0)$  are dependent on resolution; from the grid spacing used in the simulations here and the convergence tests performed with Type II critical behavior in [42], we expect the values of  $\sigma$  are accurate to a few percent. Please see [42] for further information on tests demonstrating our numerical scheme's validity and its second-order rate of convergence



in regions devoid of shocks.

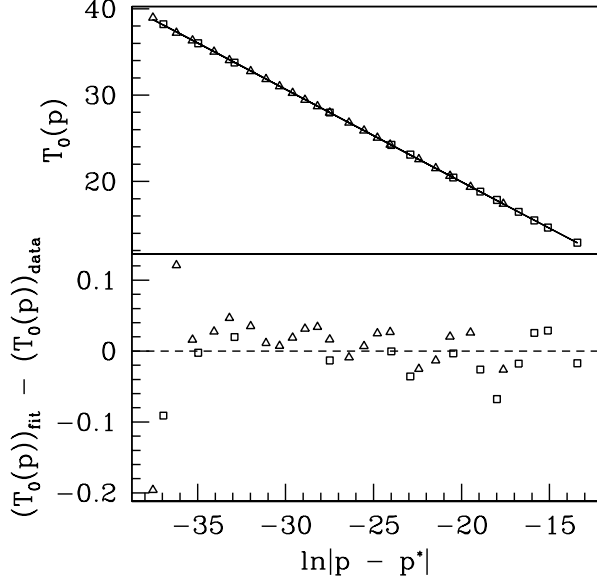


FIG. 15: (top) Lifetimes,  $T_0(p)$ , for solutions near the threshold that start from a star with  $\rho_c = 0.14$ . (bottom) Deviations of  $T_0(p)$  from the best linear fit to the data. The scaling exponent,  $\sigma$ , is found from the negative of the slope of the best linear fit to the points. The fact that both supercritical (triangles) and subcritical (squares) solutions can be used for calculating  $T_0(p)$  is illustrated here by our inclusion of both sets of points. The lifetimes shown here are actually those measured at spatial infinity; see the text for further information.

In practice, the lifetime is determined using the proper time elapsed at spatial infinity,  $T_\infty$ , instead of that measured at the origin. Let us denote  $\sigma_\infty$  as the scaling exponent measured with  $T_\infty$ . In order to get the correct scaling exponent, which would correspond to  $1/\omega_{Ly}$  of the unstable mode,  $\sigma_\infty$  must be rescaled. Since  $T_\infty$  is the same as our coordinate time,  $t$ , then

$$dT_0(t) = \alpha(0, t) dt \quad . \quad (42)$$

In order to estimate the rescaling factor, we assume that  $\alpha(0, t)$  does not vary much when the solution is in the near-critical regime, so that

$$\alpha(0, t) \approx \alpha^*(0) \quad , \quad (43)$$

where  $\alpha^*$  is the central value of the lapse of the unstable TOV solution that corresponds to the critical solution. The corrected value of  $\sigma$  is then calculated using

$$\sigma = \alpha^* \sigma_\infty \quad . \quad (44)$$

We have performed fits for  $\sigma_\infty$  and then rescaled them using the above procedure to obtain an estimate of  $\sigma$  for 55 different initial TOV stars. The Lyapunov exponent for a critical solution is  $\omega_{Ly} = 1/\sigma$ . The variation of  $\omega_{Ly}$

with  $\rho_c^*$  is shown in Fig. 16. We find that  $\omega_{Ly}(\rho_c^*)$  is fit surprisingly well by the linear relationship

$$\omega_{Ly} = 5.93\rho_c^* - 1.475 \quad . \quad (45)$$

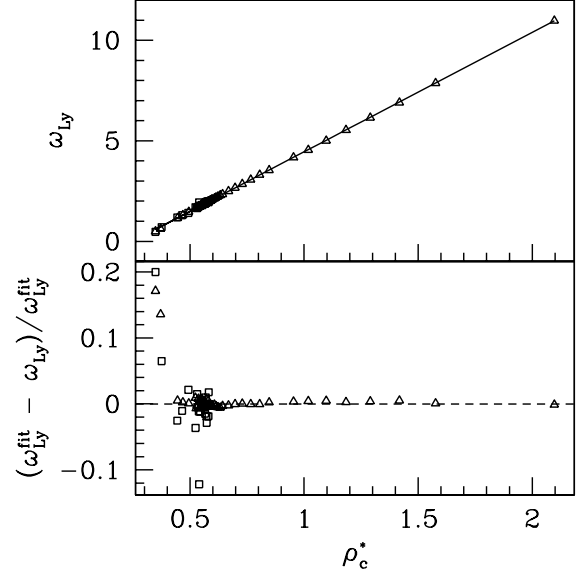


FIG. 16: (top) Real part of the estimated Lyapunov exponent for a given star solution parameterized by  $\rho_c^*$  using the first plateau (triangles) and the second plateau (squares).  $\max(2m/r)$  was used to calculate the  $\omega_{Ly}$  shown here. (bottom) The relative deviation of the data from the best linear fit to data from the first plateau (45).

In order to verify that the calculated  $\sigma$  values are, indeed, equal to  $1/\omega_{Ly}$ , we need to calculate the fundamental modes of the unstable star solutions. To the extent of the authors' knowledge and that of others [56, 57], this has not been done for the particular EOS used. However, the equations governing radial pulsations of stars in general relativity are well-known (see [58, 59] and references therein). Our method for their solution follows “Method 1-A” of [58], which exploits the fact that the equation to be solved has the Sturm-Liouville form. Since the fundamental mode,  $\omega_0$ , of these unstable star solutions is expected to be the unstable mode that we tune away, we expect  $\omega_0 = \omega_{Ly}$ . For each unstable star with  $\rho_o = \rho_c^*$ , we calculate  $\omega_0$  by iteratively integrating the eigenfunctions in first-order form from  $r = 0$  to  $r = R_*$ . After each iteration, we lower (raise) our guess for  $\omega_0$  depending on whether the solution has one (zero) nodes. This bisection process proceeds until we have found  $\omega_0$  to at least six-digits.

A comparison between  $\omega_0$  and  $\omega_{Ly}$  is shown in Fig. 17. The Lyapunov exponents deviate from the fundamental mode frequencies of unstable solutions by no more than 7% for all  $\rho_c^*$ . The relative difference,  $(\omega_0 - \omega_{Ly})/\omega_0$ , is seen to grow with  $\rho_c^*$ . This may be explained by the possible bias we mentioned earlier in how we calculate

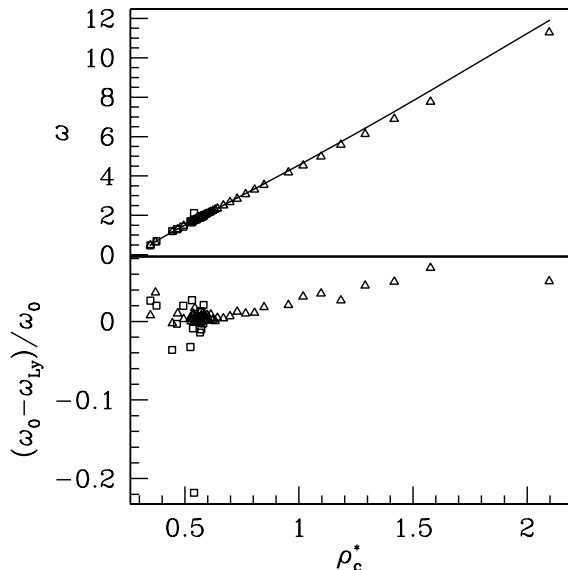


FIG. 17: (top) Comparison of  $\omega_{Ly}$  from the first plateau data (triangles) and  $\omega_{Ly}$  from the second plateau data (squares) to the fundamental mode frequencies,  $\omega_0$ , of the corresponding unstable TOV solutions (connected dots). (bottom) Relative deviations between  $\omega_{Ly}$  and  $\omega_0$ .

$\rho_c^*$  from the near-threshold solution. Stars with larger  $\rho_c^*$  oscillate with a larger amplitude that tends to decay with time (e.g. Fig. 7). If one were to assume this decay is the result of the threshold solution shedding excess kinetic energy, then our time-averages of  $\rho_o(r=0)$  would yield excessively large  $\rho_c^*$  values.

Before leaving this section, we wish to comment on the universality of our system’s critical solutions. Unlike systems with one unstable static solution—as seen in the Einstein-Yang-Mills model [23, 24], for example—the TOV system admits a family of static critical solutions (i.e. the unstable branch of TOV solutions). As demonstrated in [63–67], one can perturb *unstable* TOV solutions in a number of ways to demonstrate Type I behavior; in this kind of method, one starts with an unstable solution and tunes it to the critical solution by adjusting a parameter of the initial data that acts to eliminate the single unstable mode. In our study we demonstrate that Type I behavior of TOV solutions can also be found when one starts from a *stable* solution and tunes the perturbing agent that drives the star to the unstable branch. We have demonstrated that, at least for the perturbing methods we have explored, the mapping from stable to unstable solutions followed no obvious trend. We therefore cannot predict what critical solution a particular set of initial data will tend toward. On the other hand, the calculations performed by the others begin with initial data very near an unstable solution that is ultimately identified with a critical solution. These computations demonstrate that the unstable branch serves as a family

of 1-mode unstable solutions, whereas our method additionally demonstrates that the unstable branch is the family of 1-mode unstable solutions to which stable solutions are attracted—at least for the scenarios we examined.

## VI. CONCLUSION

In this work, we simulated spherically-symmetric relativistic perfect fluid flow in the strong-field regime of general relativity. Specifically, a perfect fluid that admits a length scale, for example one that follows a relativistic ideal gas law, was used to investigate the dynamics of compact, stellar objects. A stiff equation of state was used to approximate the behavior of some realistic state equations for NS matter. The stars served as initial data for a parameter survey, in which we drove them to collapse using either an initial velocity profile or a pulse of massless scalar field. Both types of critical phenomena were observed using each of the two mechanisms. The parameter space survey provided a description of the boundary between Type I and Type II behavior, and illustrated the wide range of dynamical scenarios involved in stellar collapse. We found that the non-black hole end states of solutions near the threshold of black hole seemed to be correlated to the type of critical behavior observed. For instance, Type I behavior seemed to always entail subcritical end states that were bound and star-like. Type II behavior, on the other hand, was observed to coincide with dispersal end states.

Since the unstable branch of TOV solutions has been known for decades, many anticipated that TOV solutions would exhibit some kind of Type I behavior. This paper describes the first in depth analysis of Type I phenomena associated with hydrostatic solutions in that the Lyapunov exponents of the critical solutions were measured for a variety of cases. We verified that the Lyapunov exponents agree well with the normal mode frequency of their associated unstable TOV solutions, confirming that the critical solutions are TOV solutions on the unstable branch. The exponents were found to follow a linear relationship as a function of the time-averaged central densities of their associated critical solutions. We also discovered that the Type I critical solutions coincided with perturbed unstable hydrostatic solutions which were typically more massive than their progenitor stars.

In the future, we hope to address a great number of topics that expand on this work. First, the supercritical section of parameter space demands further exploration in order to investigate how much matter can realistically be ejected from shock/bounce/collapse scenarios. In addition, the ability to follow spacetimes after the formation of an apparent horizon would allow us to study the possible simultaneous overlap of Type I and Type II behavior. It would also allow us to measure the ultimate mass distribution of black holes, as we are able only to measure the black hole masses at the time of formation which ne-

glects any subsequent mass accretion. Ultimately, it is our goal to expand the model a great deal, making the matter description more realistic and eliminating symmetry. As a first step, we wish to develop adaptive mesh refinement procedures for conservative systems that will be required to study critical phenomena of stellar objects in axial-symmetry [60]. Also, we wish to examine how Type II behavior changes in the context of realistic equations of state. For example, realistic equations of state effectively make the adiabatic index of the fluid a function of the fluid's density and temperature, and, to date, critical behavior in perfect fluids has only been described for fluids with constant adiabatic index.

### Acknowledgments

The authors wish to acknowledge financial support from CIFAR, NSERC, NSF PHY 02-05155, and NSF CDI AST 10-28087. SCN wishes to thank I. Olabarrieta for many helpful comments. All numerical calculations were performed on UBC's vn PIII and vnp4 clusters (supported by CFI and BCKDF).

### Appendix A: Conversion of Units and Scale

When theoretical calculations are made in the theory of general relativity, it is customary to use “geometrized units” in which  $G = c = 1$  (see App. E of [43] for a comprehensive discussion on the conversion to and from geometrized units, only a few key ideas will be mentioned here). In such units, scales or dimensions of mass ( $M$ ) and time ( $T$ ) are transformed into scales of length ( $L$ ) only, by multiplying by appropriate factors of  $G$  and  $c$ . For instance, because of how  $G$  and  $c$  scale with mass and time, one can easily derive that a quantity  $Q$  that scales like  $L^l M^m T^t$ , can be converted into geometrized units by multiplication of  $c^t (G/c^2)^m$ . After the conversion to geometrized units,  $Q$  scales as  $L^{l+m+t}$ .

Since the equations governing the ultra-relativistic fluid are all invariant under changes in the fundamental length scale  $L$ , such fluids naturally follow self-similar behavior [61]. The inclusion of  $\rho_o$  in the system eliminates this intrinsic scale-invariance via the EOS. For example, when using the polytropic EOS,  $P = K\rho_o^\Gamma$ , the constant  $K$  has dimensions  $L^{2(\Gamma-1)}$  in geometrized units and  $L^{3\Gamma-1} M^{1-\Gamma} T^{-2}$  in non-geometrized units. Hence, one may set the fundamental length scale of the system by choosing a value for  $K$  [49, 62]. Since all physical quantities are expressible in dimensions of  $L$  in geometrized units, the quantities of static *and* dynamic systems which use one set  $\{K, \Gamma\}$  should be exactly the same as those using another set  $\{\hat{K}, \hat{\Gamma}\}$ , modulo a rescaling of each quantity by the factor

$$\left(\hat{L}/L\right)^n = \left(\hat{K}^{1/2(\hat{\Gamma}-1)}/K^{1/2(\Gamma-1)}\right)^n, \quad (\text{A1})$$

where  $n$  depends on how the particular quantity scales with length. Thus, setting  $K = 1$  makes the system dimensionless, and this is the approach used in the paper. This choice simplifies the comparison of two solutions having different values of  $K$  and  $\Gamma$ .

In order to transform from our dimensionless system to one with dimensions, one must first set the scale by fixing  $K$ . Let  $\hat{X}$  be a quantity that has dimensions of  $L^l M^m T^t$ , and  $X$  be the corresponding dimensionless quantity. In order to transform  $X$  into  $\hat{X}$ , one may use the following equation

$$\hat{X} = K^x c^y G^z X, \quad (\text{A2})$$

where

$$x = \frac{l+m+t}{2(\Gamma-1)}, \quad z = -\frac{l+3m+t}{2} \quad (\text{A3})$$

$$y = \frac{(\Gamma-2)l + (3\Gamma-4)m - t}{\Gamma-1}. \quad (\text{A4})$$

When presenting results of TOV solutions using polytropic state equations, it is customary to choose  $K$  in such a way that the maximum stable mass for the given polytrope corresponds to that of the Chandrasekhar mass,  $1.4M_\odot$ . As an example, a mass  $\hat{M}(K)$  expressed in units can be calculated from the dimensionless  $M(K=1)$  via the above formula (since  $\hat{M}$  has dimensions of only mass, then  $l=0, m=1, t=0$ ):

$$\hat{M}(K) = K^{1/2(\Gamma-1)} c^3 c^{-1/(\Gamma-1)} G^{-3/2} M(K=1). \quad (\text{A5})$$

Since the TOV solutions for  $\Gamma = 2$  and  $K = 1$  yield a maximum stable mass of  $0.164$ , then the  $K$  that would make  $\hat{M}(K) = 1.4M_\odot$  would be approximately  $10^5 \text{cm}^5 \text{g}^{-1} \text{s}^{-2}$ , in cgs units. The radius of this maximum mass star is  $0.768$  with  $K = 1$ , and is about  $9.4 \text{km}$  with  $K = 10^5 \text{cm}^5 \text{g}^{-1} \text{s}^{-2}$ .

### Appendix B: Calculating the Initial Star Solution with an Ingoing Coordinate Velocity

Initializing the star with a certain coordinate velocity instead of the *Eulerian* velocity,  $v = aU/\alpha$ , couples the Hamiltonian constraint (4) and the slicing condition (7) by introducing  $\alpha$  and  $a$  into their right-hand sides. In order to explicitly show how the right-hand sides change, the conserved variables must be expressed in terms of the coordinate velocity and primitive variables via Eqs. (26-28):

$$\frac{a'}{a} = a^2 \left\{ 4\pi r \left[ \frac{\rho_o h}{1 - \left(\frac{aU}{\alpha}\right)^2} - P \right] - \frac{1}{2r^2} \right\} + \frac{1}{2r^2}, \quad (\text{B1})$$

$$\frac{\alpha'}{\alpha} = a^2 \left\{ 4\pi r \left[ \rho_o h \frac{(aU/\alpha)^2}{1 - \left(\frac{aU}{\alpha}\right)^2} + P \right] + \frac{1}{2r^2} \right\} - \frac{1}{2r^2}. \quad (\text{B2})$$

The coupling of these equations complicates their numerical solution. We will briefly describe how they are solved here. We start by solving the TOV equations, adjusting the lapse so that  $\alpha a|_{r=r_{\max}} = 1$ . Given  $U_o$ ,  $U(r)$  is specified via Eq. (41), and  $\alpha, a$  are re-calculated via a 2-dimensional Newton-Raphson method which solves Eqs. (B1-B2) at each grid point. The integration starts at the origin with  $\alpha(r=0), a(r=0)$  from the TOV solution. The Eulerian velocity,  $v = Ua/\alpha$ , is calculated using  $\alpha, a$  at this stage. Since the parameterization for  $\alpha$  is chosen at the origin, the outer boundary condition,  $\alpha a|_{r=r_{\max}} = 1$ , will not necessarily be satisfied. In order to impose this outer boundary condition and calculate the final values of  $\alpha(r)$  and  $a(r)$ , the *uncoupled* Hamiltonian constraint (4) and slicing condition (7) are then solved using the  $v$  calculated in the previous step.

### Appendix C: Perturbed Neutron Star End States

Differentiating between some of the types of outcomes is difficult. To aid in this process, we examined how various quantities varied with time at the star's radius,  $R_\star(t)$ . We define  $R_\star(0)$  as the radius of the last numerical cell before which  $\rho_o$  falls below the floor density [73], and set  $R_\star(t)$  to be the radius at which  $\rho_o(r, t) = \rho_o(R_\star(0), 0)$  to within some finite precision. This served as a fair approximation to the worldline of the fluid element originally at  $R_\star(0)$ , however, we do not assume that  $R_\star(t)$  is that of a Lagrangian observer. The Eulerian velocity at  $r = R_\star(t)$  is also considered and will be referred to as  $v_\star$ .

The boundary between SBO and O outcomes may be the most imprecisely determined one. This is due to the fact that the shock in SBO cases weakens as the perturbation is reduced, making it difficult to tell if a bounce actually happens and whether the subsequent oscillations take place about a different star solution. In addition, an O system may form a minor shock at first, but still maintain nearly-constant amplitude oscillations, indicating the absence of significant shock-heating. Herein, an O state is defined as a star which lost less than 1% of its mass over the first six periods of its fundamental mode of oscillation. This choice of cutoff is motivated by two facts: 1) evolutions which seem to be oscillating about the initial solution still lose mass, because the oscillations still eject minute amounts of matter from the star's surface; 2) those evolutions which are obviously SBO seem to eject most of the expelled matter within the first 6 oscillations. Using this definition, we estimate the systematic error of the SBO/O boundary to be no larger than 0.05 in  $v_{\min}$ .

Histories of the star's radius, change in mass, central density and velocity at its outer edge for a case that epitomizes an SBO state are plotted in Fig. 18. The star first undergoes a quick shock and bounce at its edge which seems to play an insignificant role in the subsequent evolution. This is indicated by the first maxima in  $v_\star$  near  $t \approx 3.2$ . While the shock propagates out of

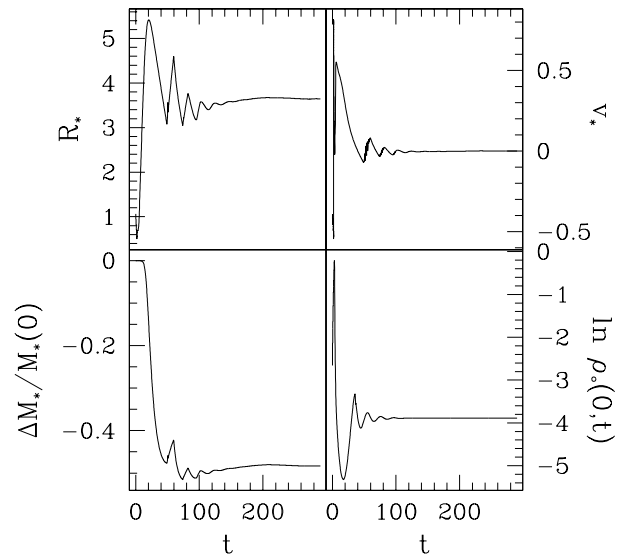


FIG. 18: Evolutions of stellar radius ( $R_\star$ ), velocity at  $R_\star$  ( $v_\star$ ), relative stellar mass deviation from initial time ( $\Delta M_\star(t)/M_\star(0)$ ), and the natural logarithm of the central density for a SBO case. The defining parameters for this run are  $\rho_o(0, 0) = 0.02$ ,  $v_{\min}(0) = 0.397$ ,  $M_\star(0) = 0.1185$ .

the star, the inner part of the star continues to infall and rebounds from the origin, which is responsible for ejecting the majority of the matter from the star. The apex of the rebound takes place near  $t = 10$ , when the star reaches minimum size and maximum central density, and when the star begins to lose a significant portion of its initial mass—up to 43% in total. This large change in  $M_\star$  signifies how poorly  $R_\star(t)$  follows the path of a Lagrangian observer in this case; however, we still feel tracking quantities along this path produces information with which we can consistently differentiate end states. In order to illustrate how the SBO star's distribution of mass changes with time, we show snapshots of  $\rho_o(r, t)$  in Fig. 19. The initial shock ( $t \simeq 1.86$ ) and bounce ( $t \simeq 2.66$ ) are clearly seen early on in the time sequence, while the subsequent rebounds of the interior are seen later in time. One can also see that the first rebound of the core ( $2.66 \lesssim t \lesssim 3.86$ ) is responsible for most of the ejection of matter, even though the initial bounce near the star's surface involves the strongest shock. The ensuing oscillations after  $t \simeq 10$  are evident in all the quantities shown. The star finally settles to a time-independent state with a smaller central density, larger radius and smaller mass than it had initially.

It is also sometimes difficult differentiating SBO states from SBD states since perturbed stars with smaller  $\rho_c$  on the SBD side near the SBD/SBO boundary often homologically inflate to arbitrary sizes. The central densities of these stars diminish to magnitudes comparable to the

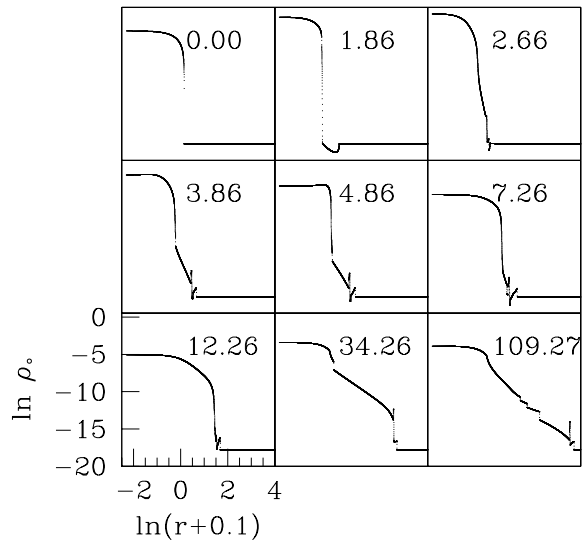


FIG. 19: Time sequence of  $\ln \rho_0(r, t)$  versus  $\ln(r+0.1)$  for the same SBO scenario shown in Fig. 18.

floor density. In contrast the denser stars close to the SBC/SBD border tend to disperse completely from the origin in a shell of matter that has compact support. In order to ensure that these “inflated” stars will not ultimately settle into a new equilibrium configuration, we typically let the evolution last until the central density of the distribution becomes comparable to the floor density and increase the size of the grid to accommodate for the expansion. If, at this time,  $v(r) > 0$  for all  $r$  and  $d\rho_0(0, t)/dt < 0$  are still satisfied, then the particular case is labeled as a dispersal, or SBD variety. An archetypal example of an SBD case involving a compact star is shown in Figs. 20–21.

The small rectangle near the upper-right corner of the SBD region in Figs. 3–4 represent 3 runs with  $\rho_c = 0.05$  that exhibited SBO behavior. It remains to be seen whether or not these cases are dominated by numerical artifacts—that is, the remnant star may converge away as  $\Delta r \rightarrow 0$ —or, if they instead represent the sparsest instances of SBD type evolutions along the black hole threshold line. If they are real solutions, then each section of the parameter space diagram may not be as homogeneous as illustrated here. Interestingly, these 3 runs are near the region where the black hole threshold behavior changes from being of Type II to Type I ( $\rho_c \approx 0.05344$ ).

Since our choice of coordinates (3) precludes a black hole from forming in finite time, we need a fairly rigorous prescription for *predicting* when they would form. Empirically, we have found that those systems which attain  $\max(2m/r) > 0.7$  will asymptote to a state that resembles a black hole in our coordinates—where  $a$  diverges and  $\alpha$  shrinks to an exponentially small magnitude at the origin. These all provide strong evidence that the sim-

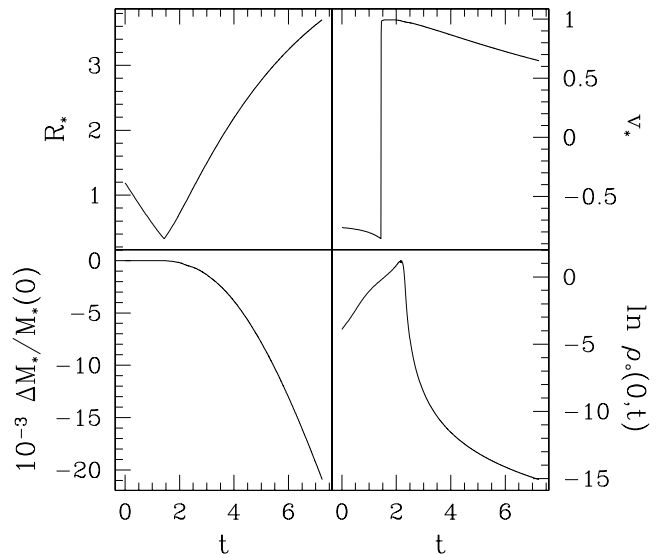


FIG. 20: Evolutions of stellar radius ( $R_*$ ), velocity at  $R_*$  ( $v_*$ ), relative stellar mass deviation from initial time ( $\Delta M_*(t)/M_*(0)$ ), and the natural logarithm of the central density for a SBD star. The defining parameters for this run are  $\rho_0(0, 0) = 0.02$ ,  $M_*(0) = 0.0726$ ,  $R_*(0) = 1.1885$ , and  $v_{\min}(0) = 0.766$ .

ulated spacetime contains a black hole. If all goes well, we label any spacetime that reaches  $\max(2m/r) > 0.995$  a “black hole”. Since such spacetimes involve extremely steep gradients, it is often difficult to stably integrate the equations of motion until this threshold is achieved. Consequently we assume that any evolution, which crashes and satisfies  $\max(2m/r) > 0.7$ , will eventually give rise to a black hole. Otherwise, the system is assumed to be one without a black hole and is either of type O, SBO or SBD.

A dynamical scenario is said to be of the type SBC if a black hole forms, a shock/bounce occurs, and  $\Delta M_*(t)/M_*(0)$  decreases over the entire course of the evolution by an amount greater than 10 times the numerical error in calculating ( $\Delta M_*(t)/M_*(0)$ ). The numerical error here is the timestep-to-timestep stochastic fluctuation we see in this quantity due to truncation and roundoff errors. The distinction between SBC and PC states is somewhat arbitrary because we are unable to measure the eventual steady-state mass of a nascent black hole, due to restrictions imposed by our coordinate system. Further, we do find a few instances where the star’s matter is still trapped even after the shock and bounce, as seen in Fig. 22. That is, the external matter bounces from the denser core, forms a shock and propagates outwards, but a portion of this matter eventually falls back onto the black hole. The fact that  $R_*$  decreases and  $v_*$  becomes ingoing after the bounce suggests that the outer parts of the star do indeed accrete onto the

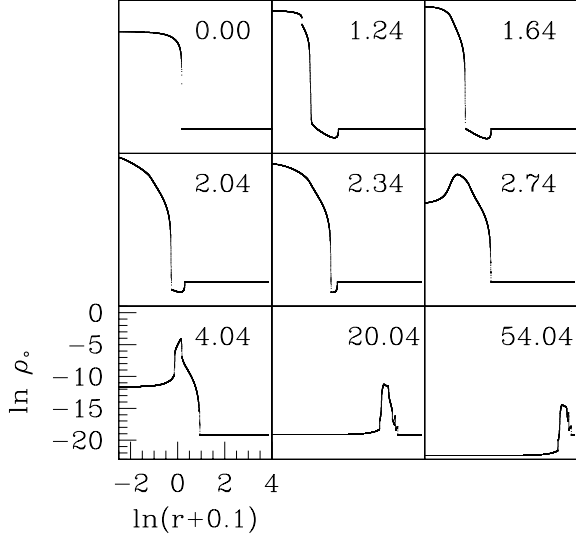


FIG. 21: Time sequence of  $\ln \rho_o(r, t)$  versus  $\ln(r + 0.1)$  for the same SBD scenario shown in Fig. 20. By  $t = 54.04$ ,  $\rho_o$  has fallen well below the floor's density in the vicinity of the origin.

collapsing interior. This example demonstrates that not all SBC scenarios result in black holes that are less massive than their progenitors, and that the final mass of the black hole is most likely continuous across the SBC/PC boundary.

For less compact stars, it is natural to justify the existence of the transition between SBD to SBO scenarios. If we follow evolutions of a particular star—say one with  $\rho_c = 0.03$ —for various  $v_{\min}$ , we see that the initial velocity perturbation results in dispersal of more and more of the stellar material as  $v_{\min}$  increases. The central densities and masses of the resultant SBO stars decrease as the SBO/SBD boundary is reached, implying that the transition is continuous. For instance, if  $\rho_c^f$  and  $M_\star^f$  are the final central density and mass, respectively, of the product star, then we should see that  $\rho_c^f, M_\star^f \rightarrow 0$  as  $v_{\min} \rightarrow v_{\min}^*(\rho_c)$ , where  $v_{\min}^*(\rho_c)$  is the threshold value of  $v_{\min}$  that separates the SBO and SBD states. We have found that this seems to be the case since after tuning  $v_{\min} \rightarrow v_{\min}^*(0.03)$  to an approximate precision of 10%,  $\rho_c^f \simeq 0.0045$ —which is about an 85% decrease in central density. Alternatively, we cross the threshold by varying  $\rho_c$  and keeping  $v_{\min}$  constant. That is, if we choose a specific  $v_{\min}$  and start perturbing stars with larger  $\rho_c$ , we see that—as the stars become less compact—the velocity distribution is able to expel more and more matter from the central core. In turn, smaller and smaller stars will form for a given  $v_{\min}$  as  $\rho_c \rightarrow \rho_c^+(v_{\min})$ , where  $\rho_c^+(v_{\min})$  is the value of  $\rho_c$  at the SBO/SBD boundary for a given value of  $v_{\min}$ . It would be interesting to calculate the scaling behavior of  $M_\star^f$  as a function of  $\rho_c - \rho_c^+(v_{\min})$

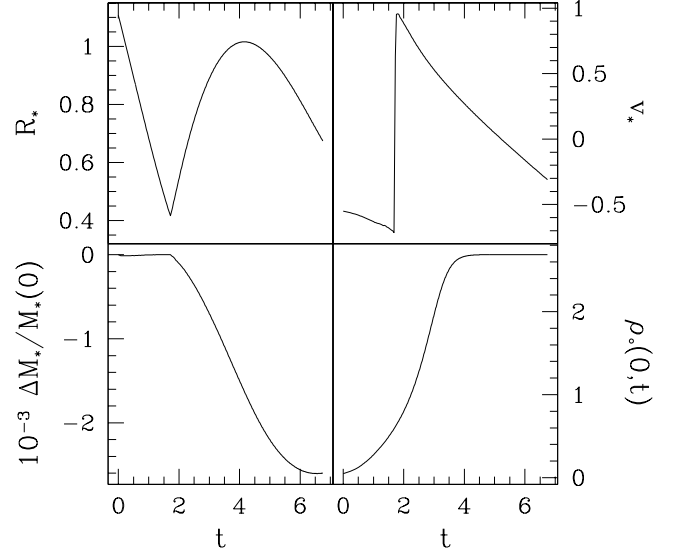


FIG. 22: Evolutions of stellar radius ( $R_\star$ ), velocity at  $R_\star$  ( $v_\star$ ), relative stellar mass deviation from initial time ( $\Delta M_\star(t)/M_\star(0)$ ), and central density for a SBC star. The evolution was stopped when the maximum value of  $2m/r$  obtained a value of 0.995, at which point the mass of black hole was calculated to be about 0.1080 and the minimum of  $\alpha$  was  $1.0 \times 10^{-8}$ . The defining parameters for this run are  $\rho_o(0, 0) = 0.05$ ,  $v_{\min}(0) = -0.556$ , and  $M_\star(0) = 0.1092$ .

or  $v_{\min}^*(\rho_c) - v_{\min}$ . An accurate calculation of this scaling law would require many runs in this regime, which is one of the most computational intensive regimes. In this limit, we would have to resolve a wide range of scales in order to evolve the initial dynamics of the compact progenitor star through to it settling into a new equilibrium. Such calculations might require a full-fledged adaptive mesh refinement (AMR) code, which we leave for future work.

#### Appendix D: Departures of Near Critical Solutions from Unstable Equilibrium

In order to gather a better understanding of what causes the near critical solutions to temporarily depart from the unstable branch, we tuned to the critical solution using different values of various control parameters. For instance, to see if the presence of the departures is affected by the floor, we tuned to the critical solution for three different values of  $\delta$ . The most marginally subcritical solutions from these searches are shown in Fig. 23. In addition, the effect of changing the outer boundary's location,  $r_{\max}$  is seen in Fig. 24. To see if the time at which the pulse collides with the star has any effect, the initial position of the pulse,  $R_\phi$  was varied; the results from this particular analysis are shown in Fig. 25.

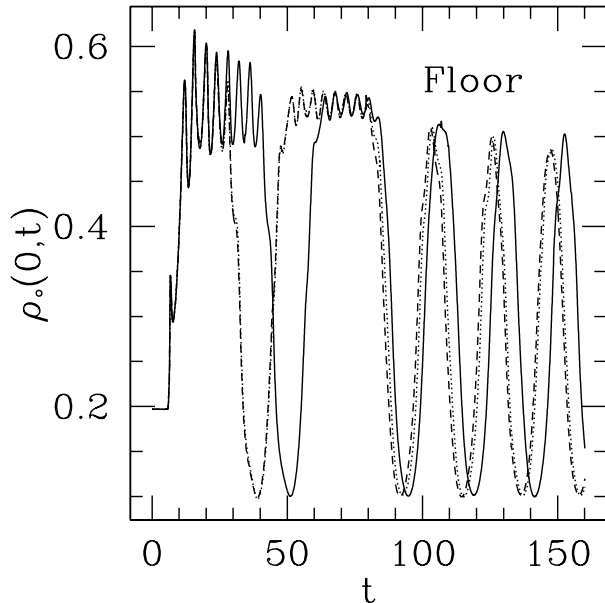


FIG. 23: Comparisons of  $\rho_o(0,t)$  for the marginally subcritical solutions obtained when using varying values of the fluid’s floor. The original, reference solution (solid curve) used  $\delta = 3.8809 \times 10^{-18}$ , while the other two lines used floor values 10 (dotted line) and 100 (dashed line) times greater. Variations can be seen between the three solutions, even though the smallest discrepancies are between the two solutions with the largest floor values. All runs shown here used  $\rho_o(0,0) = 0.197$ .

In general, we see all these aspects to have significant and non-trivial effect on the threshold solution’s departure from the unstable solution. But, all the different marginally-subcritical solutions finally depart from the unstable solution at approximately the same time and all cases share the same scaling exponent.

Whether because of its magnitude or extent, the solution’s departure seems to be affected by the floor. Increasing the size of the floor seems to hasten the initial departure; even though they represent only two points of reference, the similarity of the solutions with the two highest floor values may suggest that the floor’s effect “converges” to one behavior as its size increases. On the other hand, changes in the size of the computational domain and  $R_\phi$  seem to have no *consistent* effect on the first departure time.

The most likely explanation is that excited modes from the the artificial atmosphere surrounding the star instigate the departures. The unstable solutions to which the near critical solutions emulate are 1-mode unstable TOV solutions, and TOV solutions do not involve an atmosphere. Since these additional modes have no effect on the scaling exponent and only periodically affect the evolution of the threshold solutions, they must be transient and stable. Their little influence is consistent with the idea that they come from the atmosphere since it is hydrodynamically and gravitationally insignificant com-

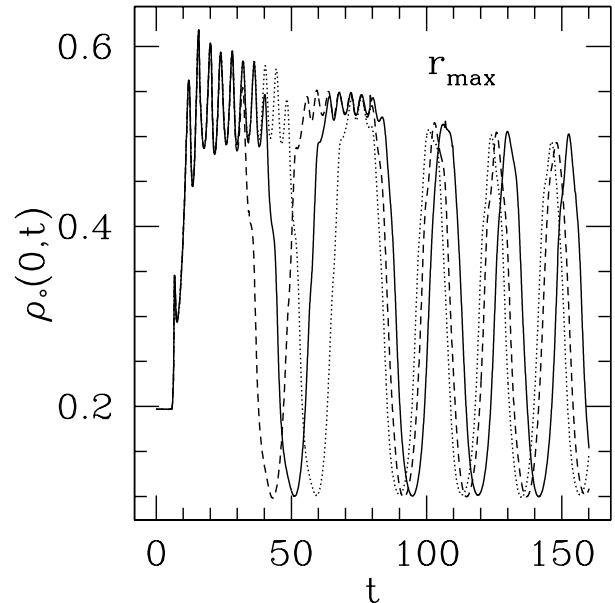


FIG. 24: Central density as a function of time of the subcritical solutions closest to the threshold obtained with physical domains of various sizes. The dotted (dashed) curve used a domain twice (thrice) as large as that of the original configuration, which is shown here as a solid curve. All runs shown here used  $\rho_c = 0.197$ .

pared to the star. Further work will need to be done in order to definitively understand the cause of the departures.

Similar studies (e.g., [63–69]) have not reported encountering similar phenomena. It remains to be seen whether it is because their investigations involved different neutron star solutions (e.g., different values of  $K$  as in [63], or rotating and magnetized unstable-branch neutron stars as in [67]), different numerical schemes, or something else altogether.

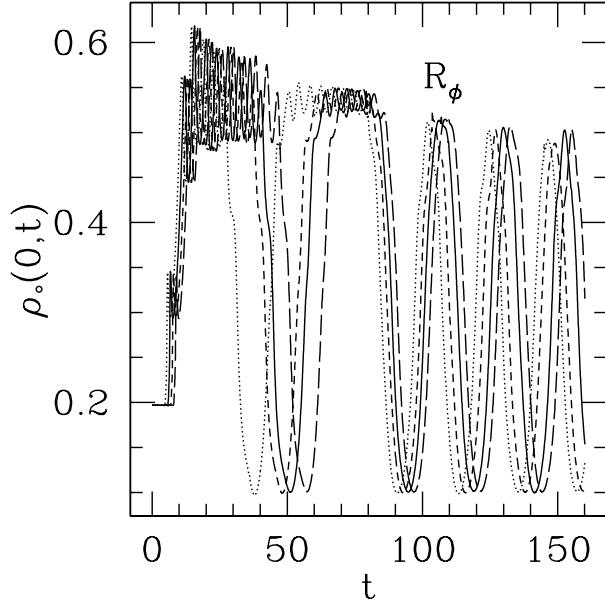


FIG. 25: Central density as a function of time of the sub-critical solutions closest to the threshold obtained by using different initial locations of the initial scalar field distribution,  $R_\phi$ . Specifically, the scalar field at  $t = 0$  takes the form of a Gaussian distribution, and the position of the center of this Gaussian is unique for each curve shown here. In our units the radius of the progenitor star was  $r = 0.87$ , while the initial positions of the scalar field pulses were at  $r = 4$  (dots),  $r = 5$  (solid curve),  $r = 6$  (short dashes),  $r = 7$  (long dashes). All runs shown here used  $\rho_c = 0.197$ .



- 
- [1] L. Zampieri, M. Colpi, S. L. Shapiro and I. Wasserman, *Astrophys. J.* , **505**, 876-896 (1998).
- [2] A. M. Green and A. R. Liddle, *Phys. Rev. D* , **60**, 063509 (1999).
- [3] I. Hawke and J. M. Stewart, *Class. Quant. Grav.*, **19**, 3687 (2002).
- [4] J. C. Niemeyer and K. Jedamzik, *Phys. Rev. Lett.* , **80**, 5481 (1998).
- [5] J. C. Niemeyer and K. Jedamzik, *Phys. Rev. D* , **59**, 124013 (1999).
- [6] J. Novak, *Astron. Astrophys.*, **276**, 606-613 (2001).
- [7] S. L. Shapiro and S. A. Teukolsky, *Astrophys. J.* , **235**, 199-215 (1980).
- [8] T. W. Baumgarte, S. L. Shapiro, and S. A. Teukolsky, *Astrophys. J.* , **443**, 717-734 (1995).
- [9] W. C. Hernandez, Jr. and C. W. Misner, *Astrophys. J.* , **143**, 452-464 (1966).
- [10] E. Gourgoulhon, *Class. Quant. Grav.*, **9**, 117-125 (1992).
- [11] E. Gourgoulhon, *Astron. Astrophys.*, **252**, 651-663 (1991).
- [12] M. M. May and R. H. White, *Phys. Rev.*, **141**, 1232-1241 (1966).
- [13] K. A. Van Riper, *Astrophys. J.* , **221**, 304-319 (1978).
- [14] J. A. Pons, S. Reddy, P. J. Ellis, M. Prakash, and J. M. Lattimer, *Phys. Rev. C* , **62**, 035803 (2000).
- [15] M. W. Choptuik, *arxiv:gr-qc/9803075*, (1998).
- [16] C. Gundlach and J. M. Martin-Garcia *Living Reviews*, <http://www.livingreviews.org/lrr-2007-5> (2007); *arxiv:0711.4620 [gr-qc]* (2007).
- [17] C. Gundlach, *Phys. Rep.*, **376**, 339-405 (2002).
- [18] M. W. Choptuik, *Phys. Rev. Lett.* , **70**, 9 (1993).
- [19] P. R. Brady, M. W. Choptuik, C. Gundlach, and D. W. Neilsen, *Class. Quant. Grav.*, **19**, 6359-6375 (2002).
- [20] C. R. Evans and J. S. Coleman, *Phys. Rev. Lett.* , **72**, 1782-1785 (1994).
- [21] T. Koike, T. Hara and S. Adachi, *Phys. Rev. Lett.* , **74**, 5170-5173 (1995).
- [22] D. W. Neilsen and M. W. Choptuik, *Class. Quant. Grav.*, **17**, 761-782 (2000).
- [23] M. W. Choptuik, T. Chmaj, and P. Bizoń, *Phys. Rev. Lett.* , **77**, 424-427 (1996).
- [24] M. W. Choptuik, E. W. Hirschmann, and R. L. Marsa, *Phys. Rev. D* , **60**, 124011 (1999).
- [25] I. Olabarrieta and M. W. Choptuik, *Phys. Rev. D* , **65**, 024007 (2001).
- [26] G. Rein, A. D. Rendall, and J. Schaeffer, *Phys. Rev. D* , **58**, 044007 (1998).
- [27] P. R. Brady, C. M. Chambers and S. M. C. V. Gonçalves, *Phys. Rev. D* , **56**, R6057-R6061 (1997).
- [28] S. H. Hawley and M. W. Choptuik, *Phys. Rev. D* , **62**, 104024 (2000).
- [29] P. Jetzer, *Phys. Rep.*, **220**, 163-227 (1992).
- [30] T. D. Lee and Y. Pang, *Phys. Rep.*, **221**, 251-350 (1992).
- [31] C. W. Lai and M. W. Choptuik, *arxiv:0709.0324v1 [gr-qc]* (2007).
- [32] S. H. Hawley, *private communication* (2002).
- [33] M. M. May and R. H. White, *Meth. Comp. Phys.*, **7**, 219-258 (1967).
- [34] C. W. Misner and D. H. Sharp, *Phys. Rev.*, **136**, B571-B576 (1964).
- [35] J. R. Wilson, *Astrophys. J.* , **163**, 209-219 (1971).
- [36] K. A. Van Riper, *Astrophys. J.* , **232**, 558-571 (1979).
- [37] F. Siebel, J. A. Font and P. Papadopoulos, *Phys. Rev. D* , **65**, 024021 (2001).
- [38] J. A. Font, T. Goodale, S. Iyer, M. Miller, L. Rezzolla, E. Seidel, N. Stergioulas, W. Suen, and M. Tobias, *Phys. Rev. D* , **65**, 084024 (2002).
- [39] J. R. Oppenheimer and G. M. Volkoff, *Phys. Rev.*, **55**, 374-381 (1939).
- [40] R. C. Tolman, *Relativity, Thermodynamics and Cosmology* (Oxford University Press, 1934).
- [41] R. C. Tolman, *Phys. Rev.*, **55**, 364-373 (1939).
- [42] S. C. Noble and M. W. Choptuik, *Phys. Rev. D* , **78**, 064059 (2008).
- [43] R. M. Wald, *General Relativity* (University of Chicago Press, Chicago, 1984).
- [44] R. Arnowitt, S. Deser, and C. W. Misner, in *Gravitation: an Introduction to Current Research*, edited L. Witten (John Wiley & Sons, New York, 1962).
- [45] F. Banyuls, J. A. Font, J. M<sup>a</sup> Ibáñez, J. M<sup>a</sup> Martí, and J. A. Miralles, *Astrophys. J.* , **476**, 221-231, (1997).
- [46] J. A. Font, *Living Reviews*, <http://www.livingreviews.org/lrr-2003-4> (2003).
- [47] D. W. Neilsen and M. W. Choptuik, *Class. Quant. Grav.*, **17**, 733-759 (2000).
- [48] J. V. Romero, J. M<sup>a</sup> Ibáñez, J. M<sup>a</sup> Martí, and J. A. Miralles, *Astrophys. J.* , **462**, 839-854 (1996).
- [49] G. B. Cook, S. L. Shapiro, and S. A. Teukolsky, *Astrophys. J.* , **398**, 203-223 (1992).
- [50] S. L. Shapiro and S. A. Teukolsky, *Black Holes, White Dwarfs, and Neutron Stars* (John Wiley & Sons, New York, 1983).
- [51] S. C. Noble, Ph.D. thesis, The University of Texas at Austin, 2003; *arxiv:gr-qc/0310116* (2003).
- [52] B. K. Harrison, K. S. Thorne, M. Wakano, and J. A. Wheeler, *Gravitation Theory and Gravitational Collapse* (The University of Chicago Press, Chicago and New York, 1965).
- [53] R. L. Marsa and M. W. Choptuik, *The RNPL Reference Manual*, <http://bh0.physics.ubc.ca/People/marsa/rnpl/refman/refman.html> (1995); *The RNPL User's Guide*, [http://bh0.physics.ubc.ca/People/marsa/rnpl/users\\_guide/users\\_guide.html](http://bh0.physics.ubc.ca/People/marsa/rnpl/users_guide/users_guide.html) (1995).
- [54] K. A. Van Riper and W. D. Arnett, *Astrophys. J.* , **225**, L129-L132 (1978).
- [55] M. Liebendörfer, A. Mezzacappa, F.-K. Thielemann, O. E. B. Messer, W. R. Hix, and S. W. Bruenn, *Phys. Rev. D* , **63**, 103004 (2001).
- [56] L. Lindblom, *private communication* (2004).
- [57] N. Stergioulas, *private communication* (2004).
- [58] J. M. Bardeen, K. S. Thorne and D. W. Meltzer, *Astrophys. J.* , **145** (1966).
- [59] C. J. Misner, K. S. Thorne, and J. A. Wheeler, *Gravitation* (W.H. Freeman and Co., San Francisco, 1970).
- [60] M. W. Choptuik, E. W. Hirschmann, S. L. Liebling, and F. Pretorius, *Class. Quant. Grav.*, **20**, 1857-1878 (2003).
- [61] M. E. Cahill and A. H. Taub, *Comm. Math. Phys.*, **21**, 1 (1971).
- [62] G. B. Cook, S. L. Shapiro, and S. A. Teukolsky, *Astrophys. J.* , **422**, 227 (1994).
- [63] K.-J. Jin and W.-M. Suen, *Phys. Rev. Lett.* , **98**, 131101

- (2007).
- [64] M.-B. Wan, K.-J. Jin, and W.-M. Suen, arXiv:0807.1710 (2008).
  - [65] M.-B. Wan, *Class. Quant. Grav.*, **28**, 155002 (2011).
  - [66] M.-B. Wan, Ph.D. thesis, Washington University in St. Louis, 2009; arXiv:1001.1427 (2010).
  - [67] S. Liebling, L. Lehner, D. Neilsen, C. Palenzuela, *Phys. Rev. D*, **81**, 124023 (2010).
  - [68] D. Radice, L. Rezzolla, T. Kellerman, *Class. Quant. Grav.*, **27**, 235015 (2010).
  - [69] T. Kellerman, L. Rezzolla, D. Radice, *Class. Quant. Grav.*, **27**, 235016 (2010).
  - [70] D. Radice, L. Rezzolla, *Phys. Rev. D*, **84**, 024010 (2011).
  - [71] A prescription for numerically solving the TOV equations can be found in [50].
  - [72] Since Novak uses  $K = 0.1$  and since  $\rho_c$  scales as  $K$ , then we may compare our values to his by multiplying 0.1 to his unitless density,  $n_B$ .
  - [73] As do many computational fluid dynamics codes, our numerical scheme prevents non-positive density and pressure values from arising by imposing minimum, positive values on these quantities. We call this the “floor” or “floor state.” See [42] for further details.